

Fault-zone controls on the spatial distribution of slow-moving landslides

Joel S. Scheingross^{1,†}, Brent M. Minchew², Benjamin H. Mackey^{1,§}, Mark Simons², Michael P. Lamb¹, and Scott Hensley³

¹*Division of Geological and Planetary Sciences, California Institute of Technology, Pasadena, California 91125, USA*

²*Seismological Laboratory, Division of Geological and Planetary Sciences, California Institute of Technology, Pasadena, California 91125, USA*

³*Jet Propulsion Laboratory, California Institute of Technology, Pasadena, California 91109, USA*

ABSTRACT

Slow-moving landslides (earthflows) can dominate hillslope sediment flux and landscape erosion in hilly terrain with mechanically weak, fine-grained rock. Controls on the occurrence of slow-moving landslides are poorly constrained and need to be understood for landscape evolution models, sediment budgets, and infrastructure and hazards planning. Here, we use airborne interferometric synthetic aperture radar (InSAR) and aerial photographs to document 150 previously unidentified active earthflows along the central, creeping portion of the San Andreas fault, California. The earthflows move seasonally in response to winter rainfall, occur on hillslopes at ~20%–40% gradients (less than typically associated with rapid, catastrophic landslides), and have similar morphological characteristics to earthflows in different climatic and tectonic settings. Although our data extend up to 10 km from the fault trace, ~75% of detected landslides occur within 2 km of the active fault. Topographic, precipitation, and rock type metrics alone are not enough to explain the observed spatial distribution of earthflows. Instead, we hypothesize that earthflows cluster near the creeping San Andreas fault because of a fault-induced zone of reduced bulk-rock strength that increases hillslope susceptibility to failure. In addition, similar lithology, topography, and climate exist north of the creeping section of the fault, yet earthflows there are rare. This may be due to large-magnitude earthquakes episodically triggering coseismic rapid landslides, which preferentially remove weak rock from the fault damage zone. Our analysis suggests

that the necessary conditions for earthflow formation in central California include some combination of reduced rock strength, fine-grained sedimentary rock, threshold precipitation and relief, and possibly the absence of large-magnitude earthquakes. These conditions likely hold for earthflow development in other areas, and our work suggests that local variations in rock strength and seismicity, such as those associated with fault zones, need to be taken into account in order to accurately predict earthflow occurrence.

INTRODUCTION

In areas of weak, fine-grained bedrock with low to moderate hillslope gradients, slow-moving landslides can be the primary drivers of hillslope lowering and the dominant source of sediment to river networks (Kelsey, 1978; Schwab et al., 2008; Roering et al., 2009; Mackey and Roering, 2011). The transport of sediment from hillslopes to river networks via slow-moving landslides has direct implications for fluvial erosion and river-profile evolution (e.g., Kelsey, 1978; Korup, 2006), sedimentation engineering and loading (e.g., Brown and Ritter, 1971), and aquatic habitat (e.g., Lisle, 1989; Montgomery, 2004). Furthermore, slow-moving landslides can damage roads and structures (e.g., Putnam and Sharp, 1940), and pose further hazards to property and life via mobilization into debris flows (Reid et al., 2003).

We use the terms slow-moving landslides and earthflows interchangeably to refer to active hillslope mass failures involving nonturbulent downslope movement of hillslope material, typically at rates of millimeters to meters per year (Cruden and Varnes, 1996). These landslides can exceed 5 m in depth, can deform via a combination of basal sliding and internal deformation, can be continually active for periods of years to centuries, and are distinct from rapid, catastrophic landslides that occur over periods

of seconds to minutes (e.g., Kelsey, 1978; Bovis and Jones, 1992; Coe et al., 2003; Mackey and Roering, 2011). Earthflow thickness is commonly assumed to extend to near the base of the zone of weathered bedrock (e.g., Swanson and Swanson, 1977; Trotter, 1993; Booth and Roering, 2011), resulting in transport of both weathered bedrock and soil. Since earthflows require readily available material to transport, the bedrock weathering rate may limit earthflow activity (Mackey and Roering, 2011).

While the kinematics and mechanics of individual earthflows have been studied for over 70 yr (e.g., Putnam and Sharp, 1940; Hutchinson and Bhandari, 1971; Kelsey, 1978; Keefer and Johnson, 1983; Iverson and Major, 1987; Angeli et al., 1996; Schulz et al., 2009), the controls on the spatial distribution of active earthflows are still poorly understood. In comparison, the spatial distribution of large catastrophic landslides has been widely shown to depend on uplift rates, climate, lithology, topography, rock structure, and seismicity (e.g., Keefer, 1984; Gabet et al., 2004; Roering et al., 2005). Similarly, the locations of smaller shallow landslides frequently correlate with soil depth, drainage area, convergent topography, intense precipitation, and removal of vegetation (e.g., Montgomery and Dietrich, 1994; Dietrich et al., 1995; Montgomery et al., 2000; Schmidt et al., 2001). Although slow-moving landslides are known to preferentially occur in Mediterranean-type climates with moderate hillslope gradients and mechanically weak sedimentary rock (e.g., Kelsey, 1978; Keefer and Johnson, 1983), there are numerous landscapes with these environmental conditions where active earthflows are not present, as well as mountainous areas with more extreme climates that do feature active earthflows (e.g., Angeli et al., 1996; Leprince et al., 2008; Schulz et al., 2009). Where earthflows do occur, they tend to cluster spatially (e.g., Kelsey, 1978; Keefer and Johnson, 1983), suggesting that some combination of environmental factors

[†]E-mail: jscheingross@caltech.edu

[§]Present address: Department of Geological Sciences, University of Canterbury, Christchurch, New Zealand.

is required for extensive earthflow activity (Mackey and Roering, 2011). An understanding of the controls on the spatial distribution of slow-moving landslides is needed to assess their contribution to erosion and landscape morphology, which in turn are essential inputs to landscape evolution modeling (e.g., Tucker and Hancock, 2010), geomorphic transport laws (Dietrich et al., 2003), and hazard analysis (e.g., Radbruch-Hall et al., 1982).

The spatial distribution of earthflows may be influenced by a number of geologic, biologic, climatic, and topographic factors, including, but not limited to, rock type, rock strength, bedrock fracture density, bedrock weathering rate, uplift rate, vegetation type and density, precipitation rate and intensity, hillslope azimuthal orientation (i.e., topographic aspect), and hillslope gradient (Kelsey, 1978; Keefer and Johnson, 1983; Bovis, 1985; Iverson, 1985; Zhang et al., 1993; Mackey and Roering, 2011). The majority of these variables have not been explored in a systematic way, and, in most cases, it is difficult to link earthflow distribution to a certain process. For example, several studies have noted a preference for earthflow occurrence on south-facing hillslopes (e.g., Putnam and Sharp, 1940; Kelsey, 1978; Mackey and Roering, 2011), but there are competing explanations for this dependency, including the lack of deep-rooted vegetation (Kelsey, 1978) and desiccation cracking (McSaveney and Griffiths, 1987; Mackey and Roering, 2011).

Here, we focus on two possible controls on the spatial distribution of slow-moving landslides that have not been previously explored, the influence of fault-zone damage and large-magnitude earthquakes. Discrete seismic events along faults create a near-fault zone of fractured and pulverized rock (e.g., Chester and Logan, 1986; Ben-Zion and Sammis, 2003; Dor et al., 2006; Mitchell et al., 2011; Savage and Brodsky, 2011). The width of this damage zone varies, but it can range from intense fracturing at scales of meters to hundreds of meters centered on the fault trace, with less intense fracturing extending several kilometers from the fault at the surface (e.g., Fialko et al., 2002; Ma, 2008; Finzi et al., 2009; Savage and Brodsky, 2011). Fault damage zones influence erosional processes (Wechsler et al., 2009), and one hypothesis we explore herein is that these zones may be favorable for slow-moving landslides due to reduced bulk-rock strength and the presence of bedrock fractures. However, an alternate hypothesis is that rapid, catastrophic landslides, which commonly occur following large earthquakes (e.g., Lawson, 1908; Keefer, 1984; Malamud et al., 2004b), may preferentially remove fractured and weathered rock from the fault damage zone

(e.g., Parker et al., 2011), leaving behind stronger bedrock in which earthflow formation is minimized.

To test these two competing hypotheses for fault-zone controls on the spatial distribution of earthflows, we investigated the central portion of the San Andreas fault in central California, where fault-zone damage can be isolated from large coseismic landslides due to the presence of a “creeping” section of the fault that lacks large earthquakes. We used airborne interferometric synthetic aperture radar (InSAR) to map slow-moving landslides along the creeping section of the central San Andreas fault (Fig. 1) and compared these results to (1) earthflows in northern California, which occur in a similar lithology, but under different climatic and tectonic conditions (Mackey and Roering, 2011), and (2) earthflows (or a lack thereof) along the locked section of the central San Andreas fault. We begin by providing a description of the study area and the methods employed in processing and analyzing the airborne InSAR data. Next, we present results on the morphologic characteristics of the earthflow population; seasonal changes in earthflow activity; the observed spatial distribution of active landslides in relationship to geologic, climatic, and topographic variables; and comparison to earthflows in northern California. Finally, we explore the role of reduced rock strength in the San Andreas fault damage zone as a possible mechanism for the observed earthflow spatial distribution, and compare earthflow distributions in the creeping versus locked sections of the San Andreas fault to examine the influence of large-magnitude earthquakes.

STUDY AREA

The region bounding the creeping section of the San Andreas fault in central California provides an ideal location to investigate the influence of fault damage zones and seismicity on the spatial distribution of earthflows. The area is subject to a common tectonic history and features many previously unmapped slope failures with morphologies characteristic of slow-moving landslides. The landslides occur dominantly along a narrow zone running parallel to the San Andreas fault, thus providing a long, linear swath ideal for spatial analysis (cf. Hillel and Arrowsmith, 2008). We examine the spatial distribution of active earthflows over an ~145-km-long by 22-km-wide swath parallel to (and approximately centered on) the creeping segment of the San Andreas fault (Fig. 1).

The San Andreas fault is a right-lateral strike-slip fault and is divided into locked sections that exhibit stick-slip behavior due to large-magnitude earthquakes, and a creeping

section that exhibits near continuous deformation. The creeping section of the San Andreas fault extends north-northwest from Parkfield, California, to San Juan Bautista, California, and it creeps at a rate of ~3 cm/yr (Savage and Burford, 1973; Burford and Harsh, 1980; Titus et al., 2005; Rolandone et al., 2008; Ryder and Bürgmann, 2008) (Fig. 1). North and south of the creeping section, the fault is locked and generates relatively large-magnitude earthquakes, while within the creeping section, there are small ($M_w < 4$) but frequent earthquakes (e.g., Nadeau and McEvilly, 2004).

Rock type southwest of the creeping section of the San Andreas fault consists of marine sandstones, mudstones, and shales dominantly from the Pancho Rico, Santa Margarita, and Monterey Formations. Lithology northeast of the fault consists of Franciscan mélangé, serpentinite, marine sandstone of the Etchegoin Formation, and shales of the Monterey, Gravelly Flat, and Panoche Formations (Dibblee, 2005, 2006, 2007a–2007j). The area southwest of the fault is characterized by low-relief rolling hills (up to ~200 m ridge to valley relief), while the area northeast of the fault is steeper and has higher relief (up to ~900 m ridge to valley relief), which may be due to more competent bedrock. Average annual precipitation, as measured by rain gauges, ranges from ~225 to 500 mm/yr in the study area, with higher average annual levels of precipitation northeast of the San Andreas fault (Western Regional Climate Center, 2011).

At the southern and northern extents of the San Andreas fault creeping section, seismic data sets show the presence of a low-velocity zone up to ~6 km wide at the surface, with a wider damage zone on the northeastern side of the fault (e.g., Thurber et al., 1997; Li et al., 2004; Lewis et al., 2007). This asymmetry is likely due to lithology differences on either side of the fault that induce preferential propagation directions for seismic waves (e.g., Ben-Zion and Shi, 2005; Dor et al., 2008). Electromagnetic imaging in the creeping section shows areas of low resistivity overlapping with low-seismic-velocity zones (Unsworth et al., 1999; Bedrosian et al., 2004). Both low seismic velocity and low resistivity have been inferred to represent high bedrock fracture density, which acts to reduce bulk-rock strength (Bedrosian et al., 2004; Clarke and Burbank, 2010). A fault damage zone likely exists throughout the creeping section of the San Andreas fault, as measurements of fault offset features suggest the San Andreas fault has experienced 300–320 km of cumulative displacement (compared to the ~150 km length of the creeping zone), ensuring that material currently in the creeping section has previously passed through locked portions

The centimeter-scale residual motion between aircraft repeat passes (i.e., residual interferometric baseline) that is uncompensated for using onboard metrology data is estimated from the imagery registration information between the two InSAR passes to generate geodetically useful data (Hensley et al., 2009a). Small residuals can remain after this process, but because UAVSAR maintains a very small baseline (typically less than 2 m), interferometric noise (decorrelation) is primarily due to temporal variations in the study area.

UAVSAR data are geolocated and typically averaged over a 3×12 (range \times azimuth) pixel window prior to public distribution to give a usable resolution of 5.7 m in range and 9.6 m in azimuth. Unwrapped interferograms are available with the UAVSAR repeat-pass interferometry (RPI) data, but we chose to unwrap the interferograms ourselves using the Statistical-Cost, Network-Flow Algorithm for Phase Unwrapping (SNAPHU; Chen and Zebker, 2000, 2001, 2002) software suite, because the high relief in the study area yields branches of low interferometric correlation (high noise), which can cause the standard unwrapping algorithm used in the UAVSAR processing chain to ne-

glect large portions of usable data. We filtered the interferograms using the Goldstein-Werner filtering method (filtering exponent = 0.5, filtering window = 3×3 , and interferometric correlation estimation window = 5×5 ; Goldstein and Werner, 1998) prior to unwrapping with SNAPHU, and we excluded data that have interferometric correlation values less than 0.3 (Rosen et al., 2000; Simons and Rosen, 2007).

EARTHFLOW MORPHOLOGY AND BULK CHARACTERISTICS

Methods

Even with high-resolution imagery and topographic data, it can be difficult to differentiate between active and dormant earthflows, which can retain morphological signatures of movement long after flowing has ceased (Mackey et al., 2009; Mackey and Roering, 2011). To objectively identify active features, we mapped landslides within the spatial extent of UAVSAR line 14003 (heading 140° from north), which runs parallel to the creeping section of the San Andreas fault (Fig. 1; Table 1). We also used ~ 1 m² resolution aerial photographs (Bing

Maps, <http://www.bing.com/maps/>), which are accurately orthorectified within ESRI ArcMap 10, and a 10-m-resolution (National Elevation Dataset [NED], <http://ned.usgs.gov/>) digital elevation model (DEM) with vertical accuracy of 2.4 m (Gesch et al., 2002; Gesch, 2007). Because InSAR measurements are only sensitive to the component of motion along the radar line-of-sight (LOS), we examined an additional 30 interferograms generated from UAVSAR flight lines that were flown perpendicular to the San Andreas fault (Table 1). We note that the majority of active landslides documented herein are observable in the interferograms formed from UAVSAR flight line 14003. The high-resolution of airborne InSAR and ability to fly at any desired heading allows documentation of deformation on small active earthflows (>50 m in width). The data set includes three different lines of sight covering different lengths of time (~ 0.5 yr to almost 2 yr repeat-pass time).

We identified active landslides as areas that showed a departure from the background interferogram phase and were coincident with morphometric features (observed in high-resolution aerial images) indicative of slow-moving landslides (e.g., lateral margins, pressure ridges,

TABLE 1. UNINHABITED AERIAL VEHICLE SYNTHETIC APERTURE RADAR (UAVSAR) INTERFEROGRAMS USED IN THIS STUDY

Line ID	Heading ($^\circ$)*	Start date	End date	Days elapsed	Full interferogram ID [†]
San Andreas fault—parallel interferograms					
14003	140	17-Nov-09	16-Nov-10	363	SanAnd_14003_09091-005_10081-014_0363d_s01_L090_01
14003	140	11-May-10	16-Nov-10	189	SanAnd_14003_10037-011_10081-014_0189d_s01_L090_01
14003	140	16-Nov-10	12-Jul-11	238	SanAnd_14003_10081-014_11048-021_0238d_s01_L090_01
14003	140	11-May-10	12-Jul-11	427	SanAnd_14003_10037-011_11048-021_0427d_s01_L090_01
San Andreas fault—perpendicular interferograms					
05008	50	26-Oct-09	18-Nov-10	363	SanAnd_05008_09085-004_10082-012_0388d_s01_L090_01
05008	50	26-Oct-09	13-Jul-11	189	SanAnd_05008_09085-004_11049-009_0625d_s01_L090_01
05008	50	23-Feb-09	3-May-10	238	SanAnd_05008_09008-005_10034-003_0434d_s01_L090_01
05010	50	3-May-10	21-Apr-11	427	SanAnd_05010_10034-005_11015-009_0353d_s01_L090_01
05010	50	26-Oct-09	18-Nov-10	387	SanAnd_05010_09085-006_10082-010_0387d_s01_L090_01
05010	50	23-Feb-09	3-May-10	434	SanAnd_05010_09008-003_10034-005_0434d_s01_L090_01
05010	50	23-Feb-09	18-Nov-10	633	SanAnd_05010_09008-003_10082-010_0633d_s01_L090_01
05012	50	3-May-10	21-Apr-11	353	SanAnd_05012_10034-007_11015-007_0353d_s01_L090_01
05012	50	26-Oct-09	18-Nov-10	387	SanAnd_05012_09085-008_10082-008_0387d_s01_L090_01
05014	50	18-Nov-10	21-Apr-11	154	SanAnd_05014_10082-006_11015-005_0154d_s01_L090_01
05014	50	26-Oct-09	18-Nov-10	387	SanAnd_05014_09085-010_10082-006_0387d_s01_L090_01
05016	50	18-Nov-10	21-Apr-11	154	SanAnd_05016_10082-004_11015-003_0154d_s01_L090_01
05016	50	26-Oct-09	18-Nov-10	387	SanAnd_05016_09085-012_10082-004_0387d_s01_L090_01
05016	50	26-Oct-09	21-Apr-11	541	SanAnd_05016_09085-012_11015-003_0541d_s01_L090_01
05016	50	20-Feb-09	18-Nov-10	635	SanAnd_05016_09007-018_10082-004_0635d_s01_L090_01
05018	50	18-Nov-10	21-Apr-11	154	SanAnd_05018_10082-002_11015-001_0154d_s01_L090_01
05018	50	13-Nov-09	18-Nov-10	370	SanAnd_05018_09089-001_10082-002_0370d_s01_L090_02
05020	50	13-Nov-09	18-Nov-10	370	SanAnd_05020_09089-003_10082-000_0370d_s01_L090_01
05022	50	13-Nov-09	16-Nov-10	367	SanAnd_05022_09089-005_10081-001_0367d_s01_L090_01
05022	50	13-Nov-09	12-May-11	544	SanAnd_05022_09089-005_11027-010_0544d_s01_L090_01
05024	50	13-Nov-09	16-Nov-10	367	SanAnd_05024_09089-007_10081-003_0367d_s01_L090_01
23009	230	3-May-10	21-Apr-11	353	SanAnd_23009_10034-004_11015-010_0353d_s01_L090_01
23011	230	3-May-10	21-Apr-11	353	SanAnd_23011_10034-006_11015-008_0353d_s01_L090_01
23011	230	26-Oct-09	18-Nov-10	387	SanAnd_23011_09085-007_10082-009_0387d_s01_L090_01
23013	230	18-Nov-10	21-Apr-11	154	SanAnd_23013_10082-007_11015-006_0154d_s01_L090_01
23013	230	26-Oct-09	18-Nov-10	387	SanAnd_23013_09085-009_10082-007_0387d_s01_L090_01
23015	230	18-Nov-10	21-Apr-11	154	SanAnd_23015_10082-005_11015-004_0154d_s01_L090_01
23015	230	26-Oct-09	18-Nov-10	387	SanAnd_23015_09085-011_10082-005_0387d_s01_L090_01
23017	230	13-Nov-09	18-Nov-10	370	SanAnd_23017_09089-000_10082-003_0370d_s01_L090_01
23019	230	13-Nov-09	18-Nov-10	370	SanAnd_23019_09089-002_10082-001_0370d_s01_L090_01

*Heading is aircraft flight direction in degrees from north.

[†]Full interferogram ID refers to the National Aeronautics and Space Administration Jet Propulsion Laboratory identification code as listed at <http://uavsar.jpl.nasa.gov/>.

and hummocky terrain; Kelsey, 1978; Cruden and Varnes, 1996; McKean and Roering, 2004; Booth et al., 2009; Mackey and Roering, 2011). To minimize false positives in active landslide classification, we required both characteristic earthflow terrain in aerial images and motion revealed by InSAR for identification. Field reconnaissance of InSAR-identified earthflows revealed deformed roads and active highway maintenance as additional evidence of recent activity (Fig. 2). The majority of identified earthflows exhibited increased velocity during winter months, as is commonly observed for slow-moving landslides (discussed later herein), suggesting that InSAR detected true landslide

motion. Finally, we note the absence of large landslide scars within the study area, suggesting that the earthflows are not related to rapid, catastrophic landslides.

Earthflow Slope Distribution

We identified a total of 150 slow-moving landslides that were active within the study region between May 2010 and July 2011. These landslides vary in active width from ~50 to 1500 m, active length from ~100 to 2500 m, active area from ~0.005 to 2 km², and show a lognormal distribution of areal extent (Fig. 3). Mean earthflow slope (defined as the mean of all slope val-

ues calculated on a pixel by pixel basis within an earthflow) is limited to a narrow range (0.32 ± 0.1 , mean $\pm 1\sigma$ standard deviation; Fig. 4A). We interpret the narrow slope distribution of earthflows to suggest slow-moving landslides may regulate hillslope gradients and create threshold hillslopes (e.g., Carson and Petley, 1970; Burbank et al., 1996; Mackey and Roering, 2011). That is, when hillslopes exceed a threshold angle, gravitational stresses become large enough to induce earthflow activity; earthflows then advect material downslope until the hillslope gradient falls below a threshold angle, and movement ceases due to the reduction in gravitational stress. Threshold hillslopes are typically associated with rapid landsliding (e.g., Burbank et al., 1996; Larsen and Montgomery, 2012), which limit hillslope gradients to slopes of ~0.6 (~30°; e.g., Roering et al., 2001; Binnie et al., 2007; Ouimet et al., 2009), compared to earthflows which appear to limit hillslopes to much lower gradients (i.e., slopes of ~0.3).

A complication to the threshold hillslope hypothesis is our observation of earthflow slope varying inversely with landslide areal extent (Fig. 3). Assuming earthflow area scales with landslide thickness, as has been shown for rapid landslides (e.g., Larsen et al., 2010), thicker earthflows failing at lower slopes suggests that earthflows initiate movement at a threshold basal shear stress rather than a threshold slope. However, this is a second-order effect in our study area, as mean earthflow slope decreases by a factor of approximately one third over two orders of magnitude change in landslide areal extent.

We compared the slope distributions of earthflows in this study to another population of 122 slow-moving landslides within the Eel River watershed in northern California (Mackey and Roering, 2011). The Eel River watershed has similar lithology to our study site (most earthflows occur in Franciscan Complex mélangé), with ~2–3 times greater annual average precipitation rates, and slightly higher vegetation densities (Mackey and Roering, 2011). Both populations of earthflows show narrow distributions of mean earthflow slope and have statistically indistinguishable mean slope distributions ($p = 0.62$ in a two-sample t -test at 5% confidence level; Fig. 4B). The observation that earthflow populations in distinct climates and tectonic regimes have indistinguishable hillslope gradient distributions further supports the idea that earthflows set threshold hillslopes.

Earthflow Aspect Distribution

Earthflows along the San Andreas fault occur dominantly on southwest-facing slopes between ~170° and 250° aspect (Fig. 4C). The aspect

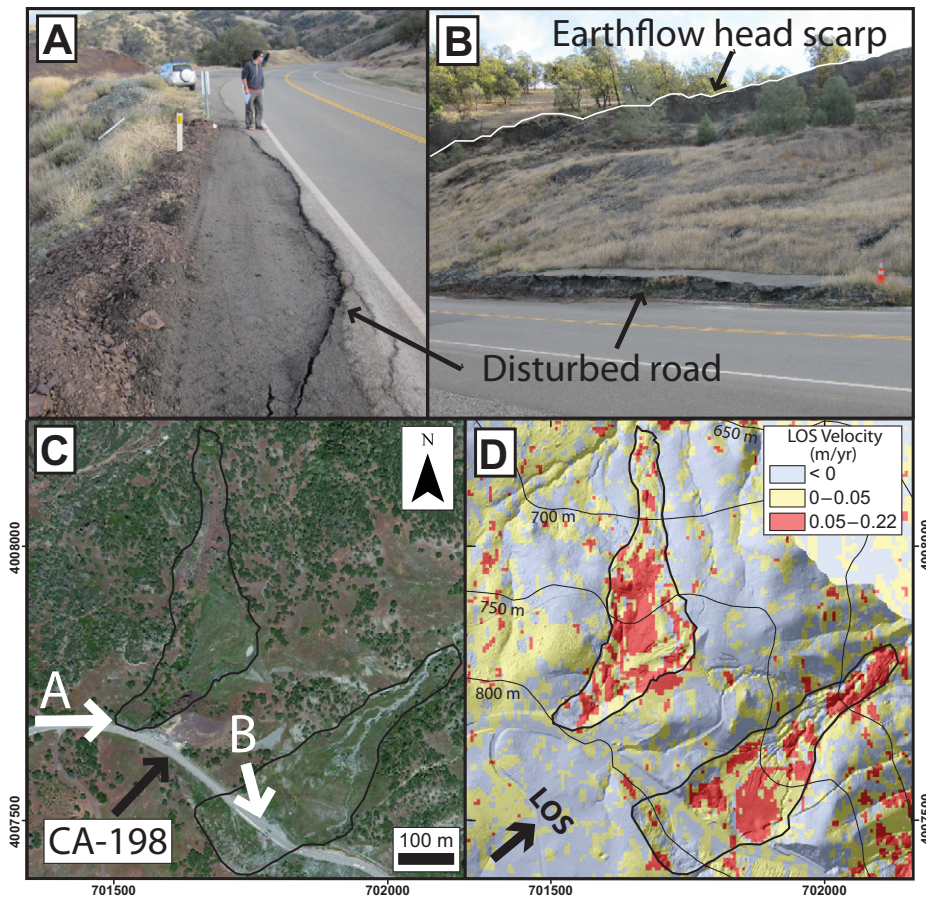


Figure 2. (A–B) Examples of deformed and fractured roads due to two separate earthflows crossing California State Highway 198. Ongoing highway maintenance confirms these earthflows are currently active. Note person and orange traffic cone for scale in A and B, respectively. (C) Bing Maps aerial photograph showing extent of earthflows (black outlines) photographed in A and B; white arrows denote location and orientation of photographs. (D) Unwrapped interferogram (line 14003, collected 16 November 2010 and 12 July 2011, 238 d elapsed between collections) showing movement of earthflows superimposed over high-resolution airborne laser swath mapping shaded relief map (obtained from OpenTopography; <http://www.opentopography.org>); black arrow indicates aircraft line-of-sight (LOS) pointing from aircraft to ground, and contours show elevation in meters above sea level. The San Andreas fault is ~850 m to the southwest from the earthflows shown. Borders on C and D show UTM coordinates, and the images are of the same areal extent.

Figure 3. Mean slope versus earthflow area and cumulative probability of earthflow area for landslides examined in this study and in Mackey and Roering (2011). Small data points show individual earthflow slopes, large points are earthflows binned into logarithmically spaced slope intervals (with 1σ error bars), and lines show cumulative probability distribution. Both the earthflows in this study and in Mackey and Roering (2011) show log-normal probability distributions of earthflow area. SAF—San Andreas fault.

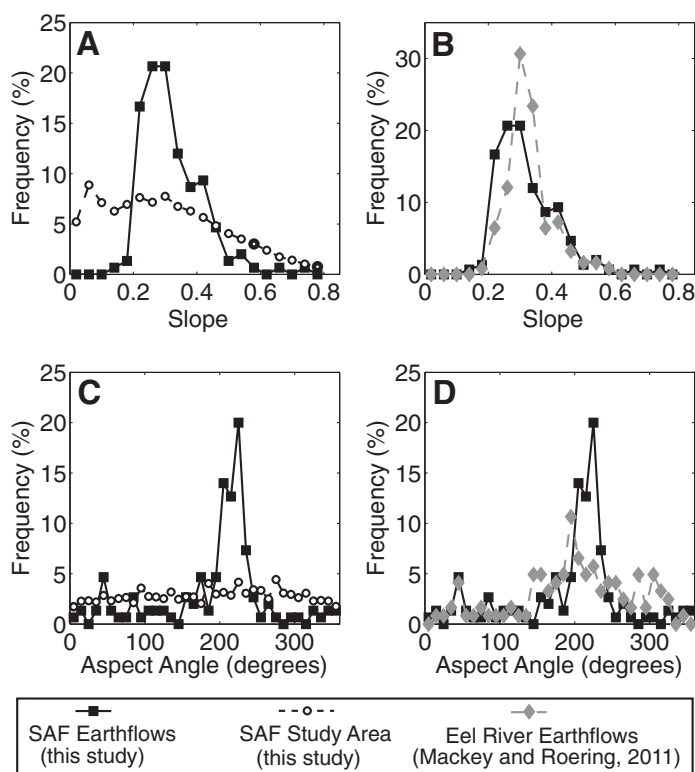
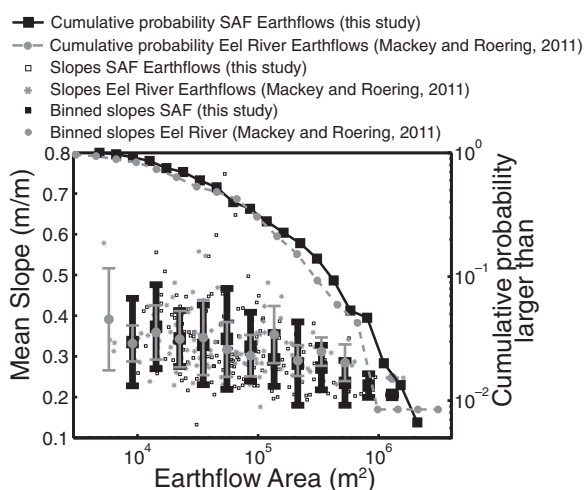


Figure 4. (A) Histogram of mean slopes of active earthflows (calculated as mean value of all slope pixels over the entire earthflow extent) compared with histogram of slopes across the entire study area. (B) Histogram of mean slopes for active earthflows in this paper (“San Andreas fault [SAF] Earthflows”) compared with those reported by Mackey and Roering (2011) (“Eel River Earthflows”). The Eel River earthflows have a slightly higher mean slope and narrower distribution (0.33 ± 0.1 , mean $\pm 1\sigma$ standard deviation) than the San Andreas fault earthflows (0.32 ± 0.1), although the populations are statistically indistinguishable ($p = 0.62$ in a two-sample t -test at 5% confidence level). (C) Histogram of average aspect for individual earthflows and the study area as a whole; $\sim 65\%$ of earthflows have aspects between 170° and 250° despite these hillslope aspects encompassing only $\sim 25\%$ of the study area. (D) Histograms of aspects for the earthflows examined in this study compared with those from Mackey and Roering (2011). For A and B, slope data are binned in 0.04 m/m bins; for C and D, aspect data are binned in 10° bins with due north equal to 0° . Both slope and aspect data were calculated from the 10-m-resolution National Elevation Dataset digital elevation model.

dependence could be influenced by the distribution of slopes adjacent to the San Andreas fault, where earthflows are most common; however, southwest-facing hillslopes only account for one third of the terrain immediately adjacent to the San Andreas fault, compared to the approximately two thirds of earthflows with average aspects between 170° and 250° (Fig. 4). Additionally, although the southwest aspect of earthflows matches the radar LOS of the line 14003 interferogram, the observed aspect dependence should not be an artifact of limited radar LOS diversity since we mapped landslides using interferograms with three different LOS directions, thereby eliminating bias due to a single imaging geometry. Southwest aspect dependence could arise due to increased solar insolation on south-facing hillslopes, which induces desiccation cracks, facilitating water flow to the earthflow failure plane (McSaveney and Griffiths, 1987; Mackey and Roering, 2011), or due to an absence of deep-rooted vegetation on south-facing hillslopes, which increases hillslope susceptibility to rapid landslides (e.g., Montgomery et al., 2000; Schmidt et al., 2001; Roering et al., 2003) and has been argued to apply to earthflows (Kelsey, 1978; Zhang et al., 1993). We note that the southwest-facing hillslopes observed here lacked trees or other deep-rooted vegetation (both on stable and active terrain), and the southwest aspect dependence of earthflows is more pronounced than that found by Mackey and Roering (2011) (Fig. 4D). This may be due to more systematic variation in vegetation cover between hillslope directions in our study area compared to that of Mackey and Roering (2011), who found no systematic difference in vegetation cover between hillslope directions in their study area, and would thus suggest that both lack of deep-rooting vegetation and increased solar insolation are important factors for predicting earthflow spatial distribution. Interestingly, Beaty (1956) noted a preference for earthflows on north-facing hillslopes near Berkeley, California, and argued that reduced solar insolation on north-facing hillslopes allowed increased moisture retention. In our study area, we see no preference for earthflows on north-facing hillslopes, suggesting that vegetation and solar insolation–induced desiccation cracking may be more important in controlling earthflow spatial distribution than moisture retention.

EARTHFLOW VELOCITIES

Methods

The study area is characterized by an increase in precipitation during winter months (Fig. 5), and comparison between the 11 May

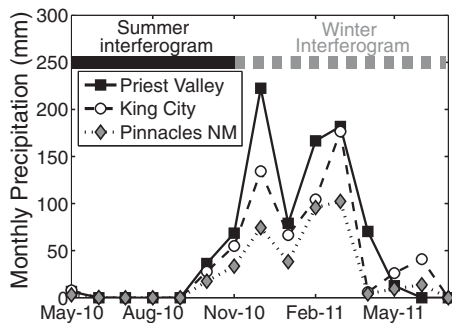


Figure 5. Monthly precipitation totals from rain gauges near the study area for May 2010–July 2011. Thick, solid black and dashed gray line marks the time period covered by the summer and winter interferogram, respectively. Note the absence of precipitation occurring over much of the summer interferogram interval, and the increased precipitation over the winter interferogram interval. See Figure 1 for rain gauge locations. NM—National Monument.

2010–16 November 2010 line 14003 interferogram (hereafter referred to as the “summer interferogram”) and the 16 November 2010–12 July 2011 line 14003 interferogram (hereafter referred to as the “winter interferogram”; see Table 1 for full interferogram identifications) allowed us to document changes in earthflow activity, spatial extent, and velocity between a relatively dry period and a relatively wet period.

LOS velocities for individual earthflows were calculated for the fault-parallel interferograms by locally subtracting the mean phase value of the area around the landslide from the unwrapped interferogram. Since InSAR only measures LOS velocity, we do not know true downslope earthflow velocities. However, the majority of landslides are oriented at similar angles with respect to the radar LOS direction, thus allowing meaningful relative comparison of LOS velocities between earthflows.

In order to examine the total number of earthflows that showed an increase in LOS velocity, we compared the distribution of the ratio v_w/v_s , where v_w and v_s are the median LOS velocity of a given landslide in the winter and summer interferogram, respectively. We excluded all areas with interferometric correlation less than 0.3 in our analysis of velocity and defined a value, a^* , representing the fraction of a given earthflow area with interferometric correlation values greater than 0.3; for example, a value of $a^* = 0.9$ means 90% of the pixels within the earthflow areal extent have interferometric correlation > 0.3 .

Seasonal Controls on Earthflow Velocity and Areal Extent

Comparisons between the winter and summer interferograms showed that both landslide velocity and areal extent tend to increase in the wetter (i.e., winter) period (cf. Calabro et al., 2010). For example, a seasonal increase in individual earthflow activity is clearly illustrated for a large landslide in the study area where we observed that the winter interferogram showed downslope movement in many portions of the earthflow not active in the summer interferogram, as well as 25%–200% increase in LOS velocity relative to the summer interferogram (Fig. 6).

We found that ~75% of earthflows showed an increase in median velocity ($v_w/v_s > 1$) between the summer and winter interferograms, with many landslides more than doubling velocity, and a maximum rate of velocity increase of $v_w/v_s = 10.2$ (Fig. 7A). The calculated increase in median velocity was not particularly sensitive to values of a^* , except at very high a^* values, where low sample size may have introduced error (Fig. 7B). We also note that when examining the 90th LOS velocity percentile, more than 80% of earthflows were interpreted to have increased in velocity in the winter interferogram, and there was a slightly stronger dependence on a^* (Fig. 7C).

We interpret the observed increase in velocity and earthflow areal extent in the winter interferogram as due to winter precipitation that increased pore-water pressure within earthflows (e.g., Iverson and Major, 1987; Schulz et al., 2009). Seasonal, precipitation-driven increases in earthflow velocity have been well documented for several individual and small groups of earthflows (e.g., Putnam and Sharp, 1940; Angeli et al., 1996; Coe et al., 2003; van Asch, 2005; Calabro et al., 2010), but no study, to our knowledge, has documented such behavior across an entire study area. The increase in areal extent of active earthflows in the wet period suggests the possibility of a yield strength, whereby portions of an individual landslide can switch between active and inactive.

SPATIAL DISTRIBUTION OF EARTHFLAWS

Methods

In order to examine controls on the spatial distribution of active earthflows along the creeping section of the San Andreas fault, we divided the study area into sets of evenly spaced fault-parallel and fault-perpendicular swaths for which we calculated zonal statistics of earthflow activity, topographic metrics, precipi-

tation metrics, and rock type. This analysis was designed to test for confounding variables that may explain the distribution of earthflows independent of the association with the San Andreas fault. The fault-perpendicular swaths were 4 km (along-fault) by 12 km (cross-fault) and extended the full ~145 km length of the study area (Fig. 8A). The fault-parallel swaths were 1 km (cross-fault) by 75 km (along-fault) extending approximately from Parkfield, California, to Bitterwater, California (Fig. 8B). Both sets of swaths were selected so that the majority of active landslides would be included within the swaths, but small enough so that landslide-prone areas and landslide-absent areas were not included within a single swath. For each swath segment, we calculated the percent of terrain that was actively deforming, the mean hillslope gradient (from the 10 m NED DEM), the fraction of southwest-facing hillslopes, the total precipitation over the study period (May 2010–July 2011, estimated for 4 × 4 km grid cells by a spatial climatic interpolation; PRISM Climate Group, Oregon State University), maximum predicted 7 d rainfall intensity for a 2 yr recurrence interval period (estimated for ~0.9 × 0.9 km grid cells by a spatial climatic interpolation; Percia, 2011), and the fraction of the dominant regional rock types (sandstone, mudstone, shale, and Franciscan mélange) exposed within each swath segment. Lithology was mapped by digitizing major units in 13 geologic maps along the San Andreas fault (Dibblee, 2005, 2006, 2007a–2007j); each unit was characterized by its dominant lithology.

In addition to these variables, we also compared measures of seismicity to earthflow occurrence within swaths along the creeping section of the San Andreas fault in order to investigate if an anticorrelation exists between large-magnitude earthquakes and earthflow activity, as suggested earlier. We used peak ground acceleration (PGA) as a ground motion variable to represent seismicity because catastrophic landslide spatial density following large earthquakes has been shown to scale with PGA (Meunier et al., 2007, 2008). We calculated PGA at 1 km² grid cells for all 3576 earthquakes ($M_w > 0.5$) that occurred between 11 May 2010 and 12 July 2011 within our study area (the time frame corresponding to line 14003 interferograms, which were used in landslide mapping), as well as for 42,731 earthquakes that occurred during a 20 yr period from 1 January 1991 to 31 December 2010. The 20 yr data set has 33 earthquakes with $M_w \geq 4$, including the 2004 Parkfield earthquake ($M_w = 6.0$). We obtained earthquake magnitudes and locations from the Northern California Earthquake Data Center (<http://quake.geo.berkeley.edu/>), and calculated PGA with a generic attenuation

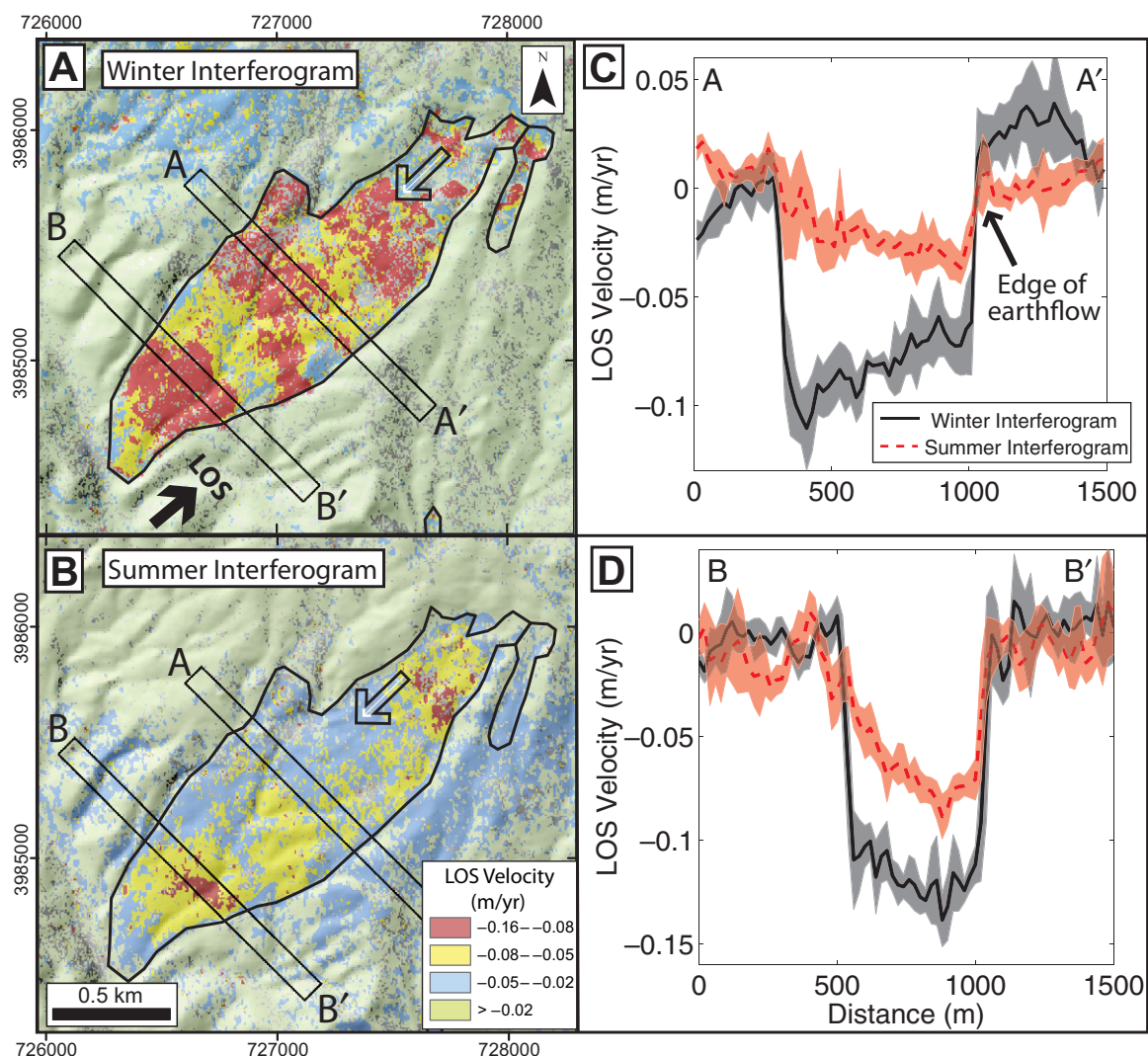


Figure 6. Line-of-sight (LOS) velocity measurements for an example earthflow for the (A) winter interferogram and (B) summer interferogram. See Figure 1B for location. LOS direction (denoted by black arrow) points from aircraft to ground, resulting in negative velocity for motion opposite to direction of the LOS. Hollow arrow denotes landslide flow direction. A-A' and B-B' boxes in A and B show areas over which LOS velocity was averaged (over 5-m-wide bins placed perpendicular to transect direction) to create velocity profiles. Comparison between (C) A-A' and (D) B-B' velocity transects shows increased velocity for the winter interferogram (black line) for both transects; shaded areas show 1σ standard deviation in velocity. Borders show UTM coordinates in A and B; speckled appearance of interferograms is due to exclusion of pixels with interferometric correlation less than 0.3.

law (Boore and Atkinson, 2007) using average shear-wave velocity values between 0 and 30 m depth (V_s30) provided by the U.S. Geological Survey for ~ 1 km² grid cells that define our PGA grid (<http://earthquake.usgs.gov/hazards/apps/vs30/>). While no attenuation law exists that is calibrated for low-magnitude earthquakes ($M_w < \sim 5.0$), the Boore and Atkinson (2007) model produces PGA values that decay with distance from the source, so that the general trends in PGA across the study area should hold, even if the exact PGA values are inaccurate. For both sets of earthquakes, we computed the median

PGA (across all earthquakes) at each grid cell and the single maximum PGA value achieved at a grid cell over the study period to compare with earthflow distribution. We chose to use maximum and median PGA in order to investigate the relative influence of single, large events versus small, frequent events, respectively.

Cross-Fault Earthflow Spatial Distribution

Active earthflows in the study area are most densely concentrated within an ~ 2 km zone on either side of the San Andreas fault between

Parkfield, California, and Bitterwater, California (Fig. 1). Approximately 60% of landslides occur within 1 km of the fault ($\sim 75\%$ occur within 2 km of the San Andreas fault), and the earthflows are slightly preferentially distributed east of the San Andreas fault (Fig. 9). This distribution may be a result of a larger fraction of southwest-facing slopes present east of the fault or from asymmetric damage zones along the fault (e.g., Dor et al., 2006; Lewis et al., 2007; Mitchell et al., 2011). North of Bitterwater, we observe nearly all earthflows are northeast of the San Andreas fault (Fig. 8A), coincident with

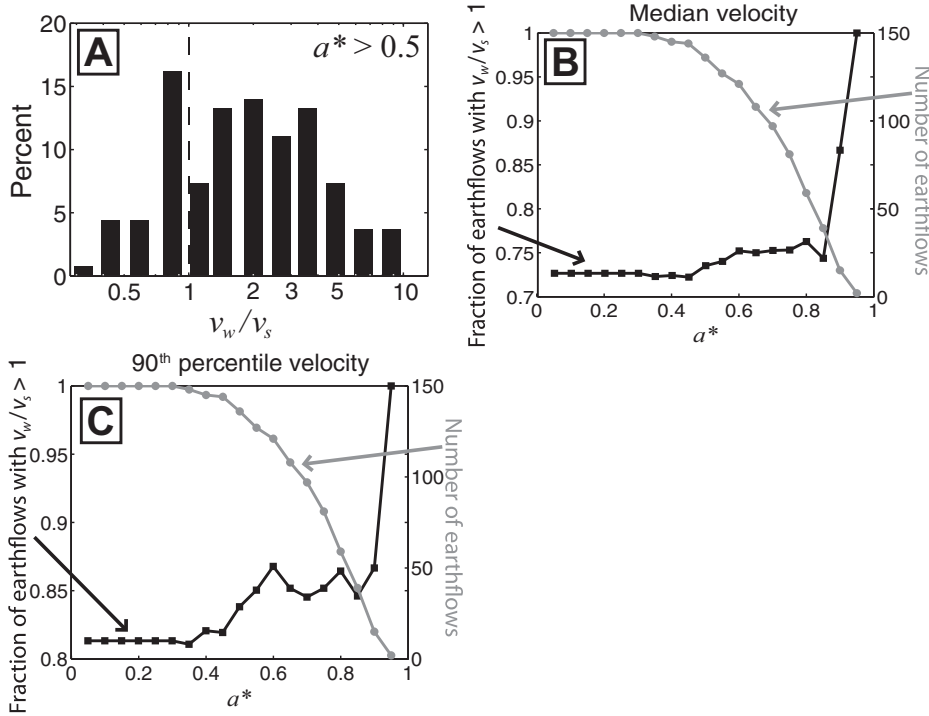


Figure 7. (A) Histogram of v_w/v_s for $a^* > 0.5$ for all earthflows, where v_w and v_s are the median line-of-sight (LOS) velocity of a given earthflow in the winter and summer interferograms, respectively, and a^* is the fraction of a given earthflow area with interferometric correlation values greater than 0.3. (B) Fraction of landslides showing higher median LOS velocities in the winter interferogram (i.e., $v_w/v_s > 1$) vs. a^* (black line). Gray line shows total number of earthflows for given a^* values. (C) Same as B, but for 90th percentile LOS velocities.

geophysical surveys that show relatively weak, fractured rock (Thurber et al., 1997; Bedrosian et al., 2004).

Zonal swath mapping parallel to the San Andreas fault allows examination of the influence of changes in topographic and climatic conditions on earthflow spatial distribution in relation to distance from the San Andreas fault. Within our fault-parallel swaths, the percent of active terrain (i.e., the percent of area occupied by earthflows within a given swath) peaks at ~7%

along the San Andreas fault, and ranges from 0% to 3% away from the San Andreas fault (Fig. 10A). Median topographic slope (over the entire area within the swath) is anticorrelated with percent of active terrain, dropping to ~0.27 along the San Andreas fault, and ranging between ~0.34 and 0.38 away from the fault (Fig. 10B). Topographic relief is small southwest of the San Andreas fault (<~300 m), increasing to maximum values of ~750 m northeast of the San Andreas fault (Fig. 10C). The percent of swath

area with southwest-facing hillslopes is similar to the percent of active terrain, with a peak at ~35% near the fault, and dropping to ~22% (the expected value if hillslope aspect is evenly distributed) away from the San Andreas fault (Fig. 10D). Annual precipitation and maximum expected 7 d rainfall intensity both show a steady increase from southwest to northeast (Fig. 10E). The distribution of the fraction of Franciscan complex (dominantly mélangé) exposed in a swath is similar to the distribution of the percent of active terrain, but there is no obvious visual correlation between other lithologies and active terrain (Fig. 10F).

We interpret none of the above metrics as sufficient to fully explain the observed cross-fault spatial distribution of earthflows. As earthflows likely suppress the development of steeper slopes (discussed earlier herein), mean hillslope gradient in earthflow-dominated areas is partially set by earthflows themselves. Thus, we discount the anticorrelation between topographic slope and earthflow activity (Figs. 10A and 10B). Hillslope aspect does not appear to be a sufficient condition to explain earthflow spatial distribution. If availability of southwest-facing aspects limits earthflow development, we would expect only a slight reduction in earthflow spatial density away from the San Andreas fault where ~20% of the landscape has southwest-facing hillslopes, not a drop to almost 0% active terrain. Threshold values of relief and precipitation are likely necessary for earthflow activity, but they are not sufficient conditions for earthflow generation, as we observe onset of earthflows coincident with increases in relief, annual precipitation, and rainfall intensity. However, we note that relief and precipitation are correlated in nature, and, furthermore, the precipitation interpolations used here employ elevation as a predictor of rainfall, thus limiting our ability to determine the influences of relief and precipitation independently. Finally, earthflows occur in several different rock types that

Figure 8. (A) Location of fault-perpendicular swaths (4 km by 12 km). (B) Location of fault-parallel swaths (1 km by 75 km). In both images, white circles show location of active earthflows, and white lines indicate location of San Andreas fault (SAF) and Calaveras/Paicines fault system. Borders show latitude and longitude in decimal degrees.

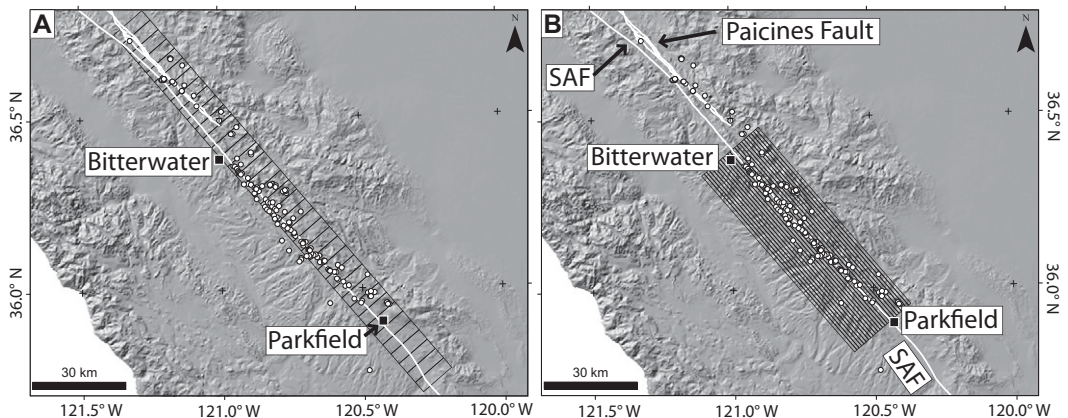
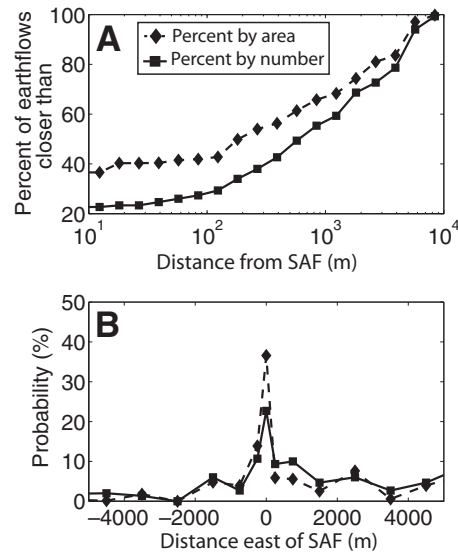


Figure 9. (A) Cumulative distribution of earthflows as a function of distance from the San Andreas fault (SAF). (B) Probability of occurrence of active earthflows on either side of the fault. Note slightly higher probability of earthflow occurrence east of the San Andreas fault, possibly corresponding to greater fault damage (see text for details). For both figures, solid line shows distribution by number of landslides, and dashed line is based on total landslide area. Distances were measured using the minimum distance between the earthflow and San Andreas fault.



exist throughout the study area; and thus lithology does not appear to be restricting earthflow extent to areas near the San Andreas fault.

We suggest that the extent of the reduced rock strength and bedrock fracturing within the fault damage zone is a primary control on the cross-fault spatial distribution of earthflows in our study area. The high density of earthflows within 2 km of the San Andreas fault is within the range of general theoretical predictions and geophysical measurements for fault damage zone widths (Thurber et al., 1997; Fialko et al., 2002; Bedrosian et al., 2004; Ma, 2008; Finzi et al., 2009), and no other morphometric or climatic variable we analyzed is sufficient to explain the cross-fault earthflow spatial distribution. Reduced rock strength and high fracture density within the fault damage zone should exist along the entire length of the San Andreas fault and its splays. Therefore, if fault damage is the determining factor affecting the presence of earthflows, we would expect to see earthflow activity outside of the creeping zone.

Along-Fault Earthflow Spatial Distribution

In the along-fault direction, the highest spatial density of earthflows occurs between Parkfield, California, and Bitterwater, California; only one active earthflow was mapped south of Parkfield (Figs. 1, 8, and 10G). North of Bitterwater, earthflows decrease in spatial density and are mostly northeast of the San Andreas fault (with some crossing the Calaveras-Paicines fault system; Figs. 1 and 8). Zonal swath mapping in the study area perpendicular to the San Andreas fault shows median topographic slope is lowest south of Parkfield, is consistently between 0.30 and 0.40 for ~100 km north of

Parkfield, and falls to ~0.22 at the northeastern extent of the study area (Fig. 10H). Maximum topographic relief is smallest south of Parkfield, and then slowly decreases (Fig. 10I). The fraction of terrain with southwest-facing aspects is scattered between ~20% and 30%, but it is generally above what is expected for an equal distribution of aspects (~22%; Fig. 10J). Annual precipitation and rainfall intensity have similar distributions to the percent of active terrain, with lows on the southwestern and northeastern extents of the creeping section, and peaks between Parkfield and Bitterwater (Fig. 10K). There is no visual correlation between the distribution of rock type and percent of active terrain (Fig. 10L). As with the fault-parallel swaths above, topographic slope, hillslope aspect, precipitation, and lithology do not appear to individually exert a strong control on the spatial distribution of earthflows.

Seismic Controls on Earthflow Spatial Distribution within the Creeping San Andreas Fault

The abrupt increase in earthflow occurrence coincident with the beginning of the creeping section of the San Andreas fault suggests that earthflow spatial distribution may be influenced by the lack of large-magnitude earthquakes in the study area. We used the fault-perpendicular swaths to test for correlation between spatial density of earthflows and seismic ground motion. There is no visual correlation of earthflow occurrence with either maximum or median PGA in both the 20 yr (1991–2011) and 427 d (May 2010–July 2011) sets of earthquakes (Fig. 11). In fact, there is a slight anticorrela-

tion between earthflow occurrence and maximum PGA for the 20 yr period (Figs. 11B and 11D). Anticorrelation between maximum PGA and earthflow occurrence is consistent with our hypothesis that coseismic landslides produced by large-magnitude earthquakes remove weak material on hillslopes, effectively limiting earthflow source material. If coseismic landslides are on average 1 m deep and the weathering rate of bedrock averages 0.5 mm/yr (DeLong et al., 2012), a large earthquake could suppress earthflow development for a period of up to 2000 yr (i.e., 1 m/0.5 mm yr⁻¹), if not longer. Under such conditions, earthquake data sets extending hundreds to thousands of years would be needed to fully capture the relationship between seismic ground motion and earthflow spatial distribution.

DISCUSSION

Mechanisms for Fault Damage Controls on Earthflow Activity

We argue that the presence of a fault damage zone is the primary control on the cross-fault distribution of earthflows within the creeping section of the San Andreas fault, and it could increase earthflow activity in three ways. First, through decreasing mechanical rock strength and thus increasing susceptibility toward hillslope failure (e.g., Molnar et al., 2007; Clarke and Burbank, 2010). Second, through creating bedrock fractures, which act as conduits for groundwater and rain flow. Fractures extending to the surface can aid in the rapid delivery of rain water to the landslide failure plane and have been suggested as a mechanism to increase pore-water pressure resulting in landslide movement (McSaveney and Griffiths, 1987; Coe et al., 2003). Third, through higher rates of weathering due to increased fracture density (e.g., Molnar et al., 2007, p. 492). Water and biological organisms, which enter bedrock through fractures, enhance weathering via hydrolysis of minerals and root development (Graham et al., 2010). As earthflow failure surfaces are commonly near the base of the zone of highly weathered bedrock (e.g., Swanson and Swanston, 1977; Trotter, 1993; Booth and Roering, 2011), this process can produce increased availability of earthflow source material and thicker earthflow deposits, thus driving earthflow activity via increased gravitational stresses. Increased weathering rates may be particularly important as earthflows have been argued to undergo long periods of inactivity while waiting for weathering processes to renew sufficient source material for movement to reinitiate (Mackey and Roering, 2011). The availability of

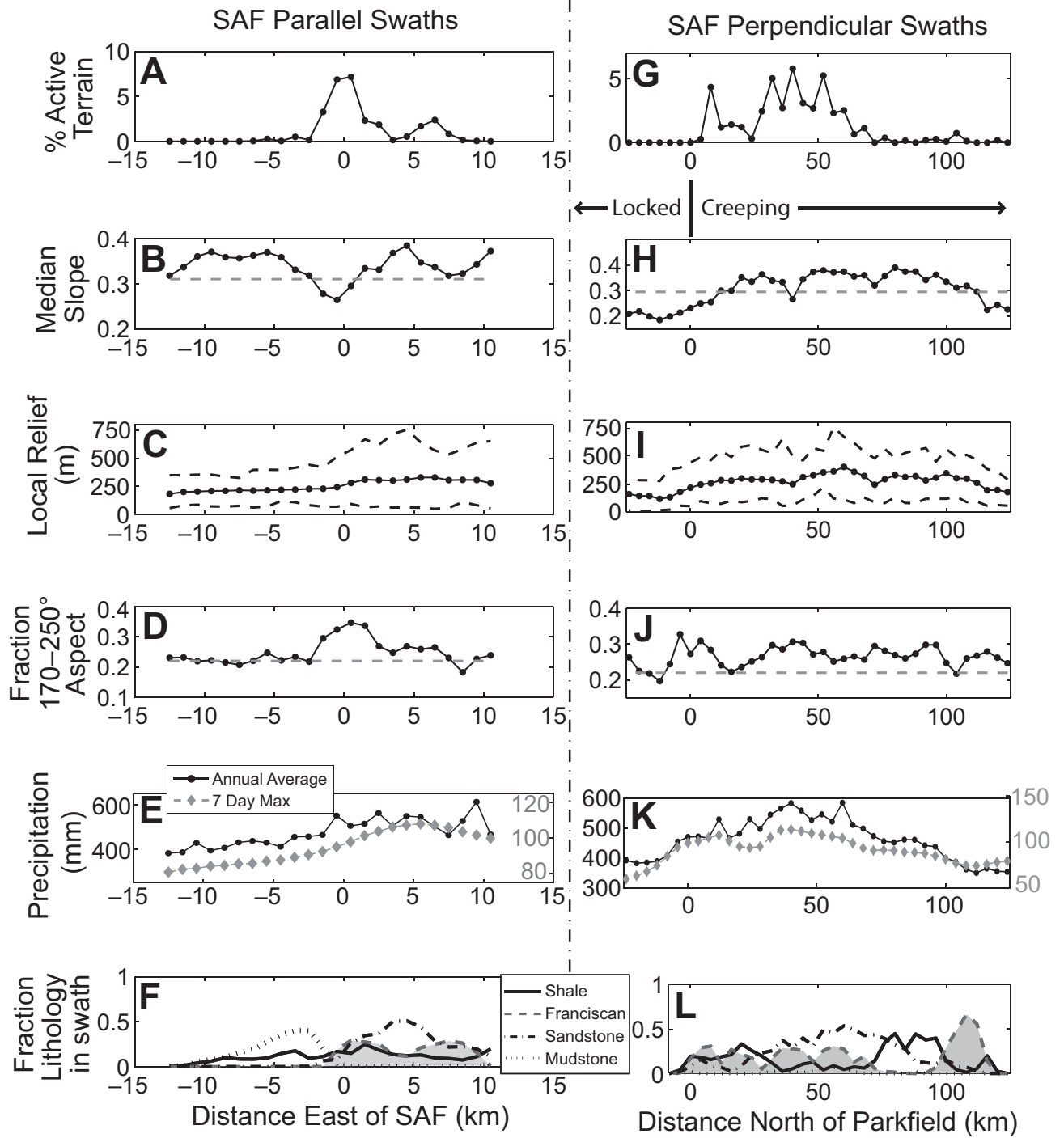


Figure 10. Summary statistics on earthflow activity and topography. (A, G) Percent of swath area covered by active earthflows. (B, H) Median local topographic slope for each swath (black line) and median slope of all active earthflows (gray dashed line). Median slope in each swath was calculated ignoring points with slopes less than 4° to reduce the effect of non-earthflow terrain (e.g., terraces), which occupied large portions of some swaths. (C, I) Average, minimum, and maximum local relief within each swath calculated with a 1-km-radius moving window. (D, J) Fraction of swath area occupied by topography with hillslope aspect between 170° and 250° (black line). Aspect range corresponds to the peak of observed active earthflow aspects (see Fig. 4C). Gray dashed line is expected fraction for evenly distributed hillslope directions. (E, K) Annual precipitation over the study period (May 2010–July 2011) as estimated by PRISM data (black line and circles, left y-axis) and 2 yr recurrence interval predicted maximum 7 d rainfall intensity as estimated by National Oceanic and Atmospheric Administration (gray line and diamonds, right y-axis) (Percia, 2011). (F, L) Fraction of lithology present in each swath for the four major lithologies classified; Franciscan is shaded gray for ease in identification. A–F are for fault-parallel swaths, and G–L are for fault-perpendicular swaths; each point represents a value for an individual swath. SAF—San Andreas fault.

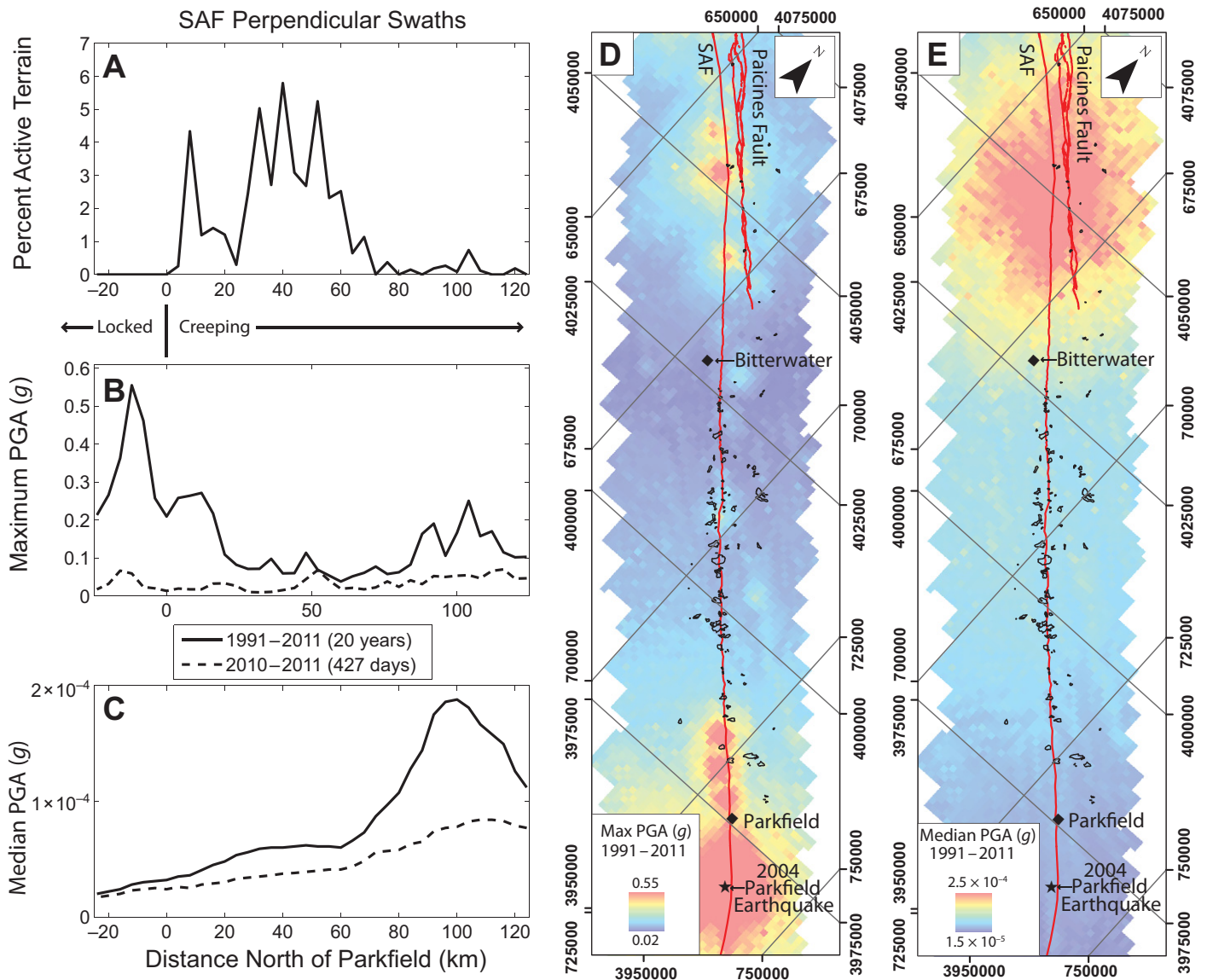


Figure 11. Association of ground motion predictions and earthflow activity. (A) Fraction of terrain composed of active earthflows for each San Andreas fault (SAF)–perpendicular swath segment (same as Fig. 10G). Maximum (B) and median (C) peak ground acceleration (PGA) estimated in each swath for all earthquakes during the 20 yr period from 1991 to 2011 (solid line) and for earthquakes corresponding to the time period of UAVSAR measurements (May 2010–July 2011, dashed line). Spatial distribution of estimated (D) maximum and (E) median PGA for the 20 yr (1991–2011) period. Black outlines show mapped landslide locations, and UTM coordinates are indicated on figure borders; note difference in color bar scale between D and E.

readily transportable material may be especially high for earthflows that cross or have heads abutting the San Andreas fault (22% of earthflows within our study area; Fig. 1B). For these earthflows, the creeping motion of the fault may drive landslide activity via lateral advection of material into the earthflow sediment source zone at rates faster than background weathering processes. That is, motion along the San Andreas fault could potentially supply source material to earthflows faster than earthflow movement depletes the available supply.

Do Large-Magnitude Earthquakes Suppress Earthflow Development?

We showed a potential anticorrelation between earthflows and maximum PGA within the creeping section of the San Andreas fault and further investigated the hypothesis that large-magnitude earthquakes inhibit earthflow development by comparing the spatial distribution of earthflows in the creeping versus northern locked section of the San Andreas fault and its major splays (the Hayward and Calaveras

faults). North of the creeping section, the San Andreas fault passes through the Santa Cruz Mountains, eventually entering the Pacific Ocean ~10 km south of San Francisco, California. Earthflows in the Santa Cruz Mountains exist (Wieczorek et al., 2007) but are rare, and the area has a high density of rapid landslides as opposed to earthflows (Nolan and Marron, 1985). Similarly, earthflows are not common within the fault damage zone of the Calaveras or Hayward faults. Keefer and Johnson (1983) summarized literature and conducted extensive

aerial and ground-based reconnaissance to identify areas of high earthflow spatial density over a large portion of the San Francisco Bay area, including the entire lengths of the Calaveras and Hayward faults. Comparing mapping by Keefer and Johnson (1983) with earthflows identified in this study shows earthflows are more continuously distributed along the creeping section of the San Andreas fault than along the Calaveras and Hayward faults (Fig. 12). While Keefer and Johnson (1983) mapped an area of high earthflow density at the northern extent of the Calaveras and Hayward faults, earthflows here extend distances up to 12 km from the fault, suggesting factors besides fault-zone damage are influencing the earthflow spatial distribution.

Both the Santa Cruz Mountains and the areas adjacent to the Calaveras and Hayward faults feature abundant exposure of Franciscan mélangé and other lithologies that have been documented to host earthflows (Jennings and Burnett, 1961; Rogers, 1966), suggesting rock type does not limit earthflow occurrence north of the creeping section. To investigate the controls of relief, hillslope gradient, aspect, and annual precipitation on earthflow spatial distribution, we performed a swath analysis similar to that presented earlier herein for the area extending ~2 km on either side of the San Andreas fault from the Transverse Ranges to the San Francisco Peninsula. These swaths showed that relief, slope, and aspect are similar between the northern locked and creeping sections of the San Andreas fault, although annual precipitation is higher in the former.

Given the similarity in lithology, topography, and climate between the northern locked and creeping sections of the San Andreas fault, we expect an equal spatial distribution of earthflows within the fault damage zones of both areas. The lack of earthflows within the fault damage zone north of the creeping section may be controlled by large-magnitude earthquakes, which induce coseismic landslides. The Santa Cruz Mountains experienced many coseismic landslides during the 1906 San Francisco earthquake ($M_w = 7.9$) and the 1989 Loma Prieta earthquake ($M_w = 6.9$) (Lawson, 1908; Keefer, 2000). Similarly, paleoseismology on the Hayward fault shows large-magnitude earthquakes have a recurrence interval of ~160 yr, with the last earthquake in 1868 ($M_w = 6.8$) (Lienkaemper et al., 2010), and that there have been 13 $M_w > 5$ earthquakes on the Calaveras fault in the past 150 yr (Oppenheimer et al., 1990; Manaker et al., 2003). Coseismic landslides associated with these large-magnitude earthquakes may preferentially remove weathered and fractured bedrock from hillslopes, thus limiting the availability of

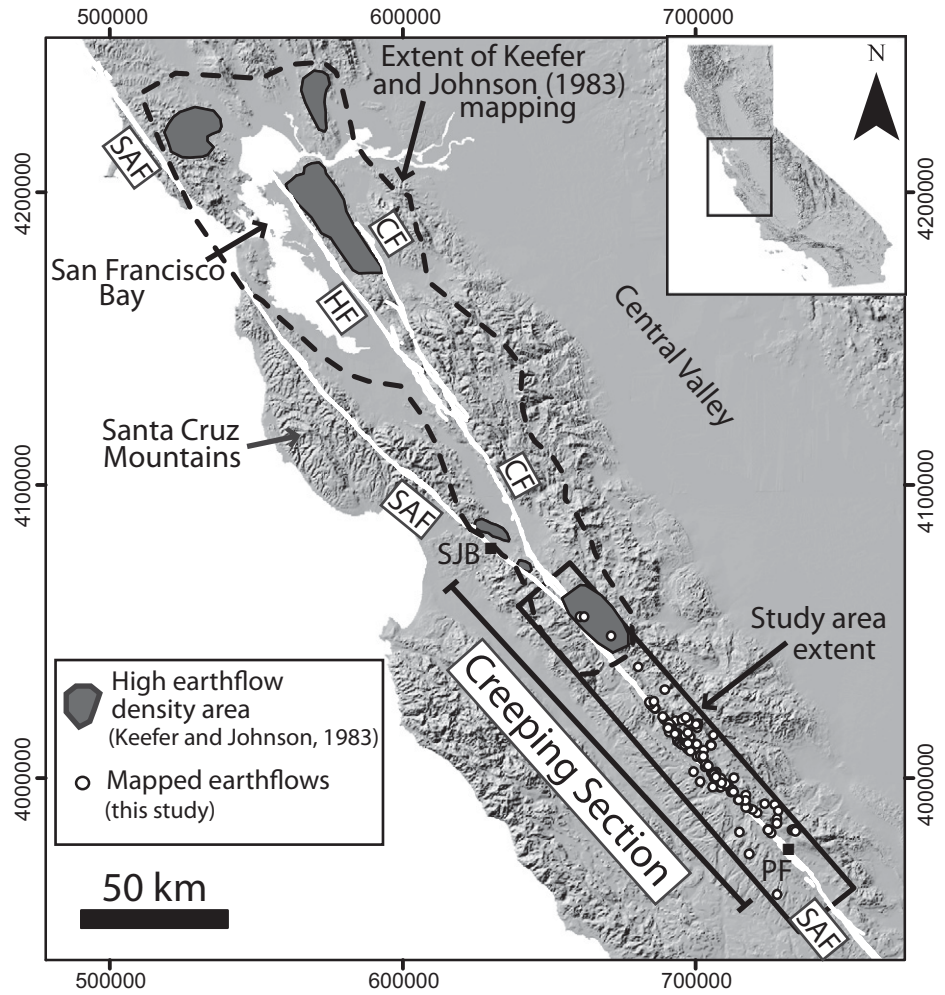


Figure 12. Map of the San Andreas fault (SAF), Calaveras fault (CF), and Hayward fault (HF) showing the location of areas of high earthflow density mapped by Keefer and Johnson (1983) as digitized from their figure 1. White dots are earthflows mapped in this study. Town abbreviations are same as Figure 1; inset shows location in California; borders show UTM coordinates in meters.

source material for earthflow transport, and suppressing earthflow development. This last point is difficult to unambiguously prove as climatic, topographic, and geologic conditions vary when moving from the creeping to the locked sections of the San Andreas fault (Fig. 13). For example, heavy rainfall associated with an El Niño year (1997–1998) produced a large number of rapid landslides in the Santa Cruz Mountains (Baum et al., 1999), suggesting that rainfall-induced shallow landsliding may also limit earthflow source material. Similarly, Keefer and Johnson (1983) showed areas of high earthflow density outside of the fault damage zone, perhaps driven by increased regional precipitation in the San Francisco Bay area, which could allow earthflow development despite increased rock strength. Ultimately, the competing influences

of topography, climate, lithology, rock strength, and seismicity all can affect earthflow spatial distribution.

Comparisons of earthflow distribution between the creeping and southern locked section of the San Andreas fault are difficult. At the southern extent of the creeping section, coseismic, rapid landslides have been documented for the 1966 and 2004 Parkfield earthquakes (both $M_w = 6.0$) (Brown et al., 1967; Rymer et al., 2006). Unfortunately, despite observing the southern extent of our mapped earthflows coincident with the onset of coseismic landslides, we were unable to test the anticorrelation of earthflows and seismicity in this region. Our swath analysis showed that relief, hillslope gradient, and precipitation decrease south of the creeping section of the San Andreas fault, as

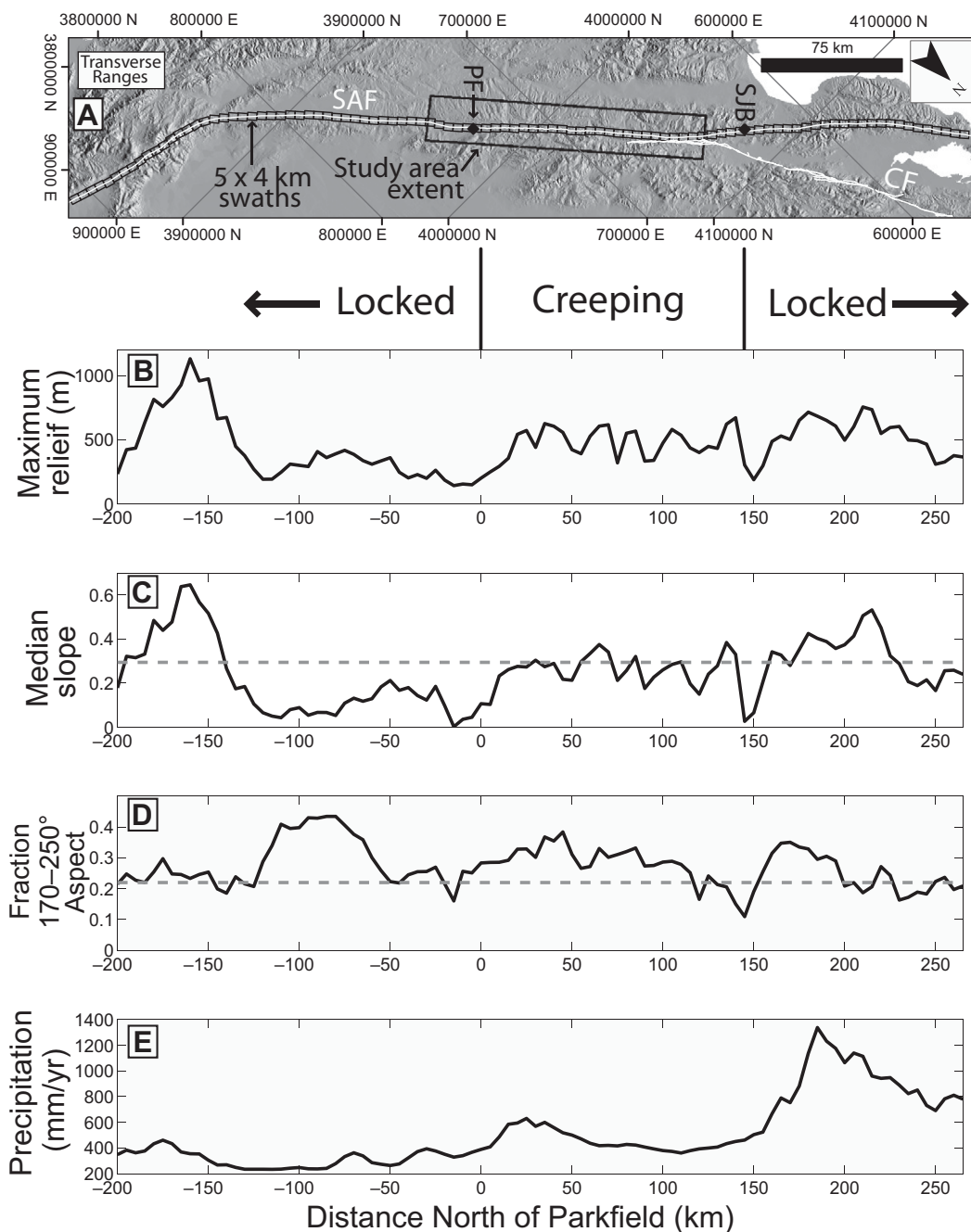


Figure 13. (A) Map of the San Andreas fault (SAF) from the Transverse Ranges (southern extent) to the San Francisco Peninsula (northern extent) showing 4 km (cross-fault) by 5 km (along-fault) San Andreas fault-centered swaths. Borders are UTM coordinates; abbreviations are same as Figure 1. Also shown are swath-wide statistics of maximum relief (B), median hillslope gradient (C), fraction of area with southwest-facing hillslopes (D), and 1971–2000 mean annual precipitation as estimated by PRISM data for $\sim 0.8 \times 0.8$ km grid cells (E). Gray dashed lines in C and D are median slope of all active earthflows and expected fraction of aspects for evenly distributed hillslope directions, respectively.

the San Andreas fault enters a broad, low-relief valley (Fig. 13). Thus, topography and climate in the southern locked section are not suitable for the generation of earthflows, regardless of the degree of seismicity.

We interpret the observed earthflow spatial distribution within the creeping section of the San Andreas fault to be a unique case where low regional precipitation and the absence of large-magnitude earthquakes limits the spatial distribution of slow-moving landslides to the reduced-rock-strength and high-fracture-den-

sity fault damage zone, thus allowing a test of rock strength and bedrock fracture controls on earthflow spatial distribution. It is possible that under changing environmental conditions (for example, increased precipitation), earthflows could become more frequent in areas outside of the fault damage zone of the creeping San Andreas fault. In such a scenario, earthflows within the fault damage zone may occur at lower slopes due to decreased rock strength.

We find that faulting introduces competing influences that can both promote and suppress the

occurrence of slow-moving landslides through reduced rock strength and large-magnitude earthquakes, respectively. These processes should be accounted for in the development of landscape evolution models and geomorphic transport laws that incorporate earthflow processes. Future work on the relative influences of tectonics, climate, topography, and lithology is needed to develop a robust model to predict the spatial distribution of earthflows, similar to previous work for shallow landslides (e.g., Montgomery and Dietrich, 1994; Dietrich et al., 1995).

CONCLUSIONS

We used a combination of airborne InSAR and high-resolution aerial images to map the occurrence and extent of active, slow-moving landslides in an ~145 by 22 km swath centered on the creeping portion of the San Andreas fault, California. The majority of mapped landslides show high interferometric correlation and display seasonal increases in line-of-sight velocity corresponding to periods of increased precipitation. The earthflows occur dominantly with mean hillslope gradients near 0.32, suggesting slow-moving landslides create threshold hillslopes at slope angles significantly lower than commonly assumed for rapid landslides. We find a strong association between earthflow occurrence and distance from the San Andreas fault, with ~75% of mapped landslides occurring within 2 km of the fault trace. This zone corresponds to theoretical predictions and field measurements of the surficial extent of the San Andreas fault damage zone. The observed spatial distribution of earthflows cannot be explained by topographic metrics, rock type, or climate alone. Instead, we suggest that the extent of the fault damage zone locally controls the spatial distribution of earthflows along the creeping section of the San Andreas fault. The fault damage zone features fractured and pulverized rock, which reduces bulk-rock strength, increases bedrock permeability, and may increase bedrock weathering rates (and hence, earthflow thickness), all of which promote earthflow activity. Earthflows occur at lower spatial densities north of the creeping section, perhaps as a result of large-magnitude earthquakes inducing coseismic landslides that suppress earthflow development via removal of earthflow source material from hillslopes. We suggest that reduced rock strength, bedrock fracturing, threshold precipitation and relief, fine-grained rock, and possibly the absence of large-magnitude earthquakes are necessary conditions for earthflow development in central California. None of these variables alone is sufficient for earthflow formation, but in certain cases, a single variable can exert a strong control.

ACKNOWLEDGMENTS

We benefited from fruitful discussions with Jean-Philippe Avouac, Jean-Paul Ampuero, and Piyush Agram. Eric Fielding, Yang Zheng, and Brian Hawkins helped facilitate Uninhabited Aerial Vehicle Synthetic Aperture Radar (UAVSAR) data access. The Keck Institute for Space Studies provided funding for this study through the Advanced Earth Surface Observation Project. Scheingross was partially supported by a National Science Foundation Graduate Research Fellowship. We thank three anonymous reviewers for insightful comments that improved the structure and clarity of this manuscript.

REFERENCES CITED

- Angeli, M.G., Gasparetto, P., Menotti, R.M., Pasuto, A., and Silvano, S., 1996, A visco-plastic model for slope analysis applied to a mudslide in Cortina d'Ampezzo, Italy: *Quarterly Journal of Engineering Geology*, v. 29, p. 233–240, doi:10.1144/GSL.QJEGH.1996.029.P3.06.
- Baum, R.L., Schuster, R.L., and Godt, J.W., 1999, Map Showing Locations of Damaging Landslides in Santa Cruz County, California, Resulting from 1997–98 El Niño Rainstorms: U.S. Geological Survey Miscellaneous Field Studies Map MF-2325-D, scale 1:125,000.
- Beatty, C.B., 1956, Landslides and slope exposure: *The Journal of Geology*, v. 64, no. 1, p. 70–74, doi:10.1086/626317.
- Bedrosian, P.A., Unsworth, M.J., Egbert, G.D., and Thurber, C.H., 2004, Geophysical images of the creeping segment of the San Andreas fault: Implications for the role of crustal fluids in the earthquake process: *Tectonophysics*, v. 385, no. 1–4, p. 137–158, doi:10.1016/j.tecto.2004.02.010.
- Ben-Zion, Y., and Sammis, C.G., 2003, Characterization of fault zones: Pure and Applied Geophysics, v. 160, no. 3–4, p. 677–715, doi:10.1007/PL00012554.
- Ben-Zion, Y., and Shi, Z.Q., 2005, Dynamic rupture on a material interface with spontaneous generation of plastic strain in the bulk: *Earth and Planetary Science Letters*, v. 236, no. 1–2, p. 486–496, doi:10.1016/j.epsl.2005.03.025.
- Binnie, S.A., Phillips, W.M., Summerfield, M.A., and Fifield, L.K., 2007, Tectonic uplift, threshold hillslopes, and denudation rates in a developing mountain range: *Geology*, v. 35, no. 8, p. 743–746, doi:10.1130/G23641A.1.
- Boore, D.M., and Atkinson, G.M., 2007, Boore-Atkinson NGA ground motion relations for the geometric mean horizontal component of peak and spectral ground motion parameters: Pacific Earthquake Engineering Research Center, PEER 2007/01: http://peer.berkeley.edu/publications/peer_reports/reports_2007/reports_2007.html (accessed March 2011).
- Booth, A.M., and Roering, J.J., 2011, A 1-D mechanistic model for the evolution of earthflow-prone hillslopes: *Journal of Geophysical Research—Earth Surface*, v. 116, F04021, doi:10.1029/2011JF002024.
- Booth, A.M., Roering, J.J., and Perron, J.T., 2009, Automated landslide mapping using spectral analysis and high-resolution topographic data: Puget Sound lowlands, Washington, and Portland Hills, Oregon: *Geomorphology*, v. 109, no. 3–4, p. 132–147, doi:10.1016/j.geomorph.2009.02.027.
- Bovis, M.J., 1985, Earthflows in the interior plateau, southwest British Columbia: *Canadian Geotechnical Journal*, v. 22, no. 3, p. 313–334, doi:10.1139/t85-045.
- Bovis, M.J., and Jones, P., 1992, Holocene history of earthflow mass movements in south-central British Columbia—The influence of hydroclimatic changes: *Canadian Journal of Earth Sciences*, v. 29, no. 8, p. 1746–1755, doi:10.1139/e92-137.
- Brown, R.D., Vedder, J.G., Wallace, R.E., Roth, E.F., Yerkes, R.F., Castle, R.O., Waananen, A.O., Page, R.W., and Eaton, J.P., 1967, The Parkfield-Cholame, California, Earthquakes of June–August 1966—Surface Geology Effects, Water-Resources Aspects, and Preliminary Seismic Data: U.S. Geological Survey Professional Paper 579.
- Brown, W.M., and Ritter, J.R., 1971, Sediment Transport and Turbidity in the Eel River Basin, California: U.S. Geological Survey Water-Supply Paper 1986, 67 p.
- Burbank, D.W., Leland, J., Fielding, E., Anderson, R.S., Brozovic, N., Reid, M.R., and Duncan, C., 1996, Bedrock incision, rock uplift and threshold hillslopes in the northwestern Himalayas: *Nature*, v. 379, no. 6565, p. 505–510, doi:10.1038/379505a0.
- Burford, R.O., and Harsh, P.W., 1980, Slip on the San Andreas fault in central California from alignment array surveys: *Bulletin of the Seismological Society of America*, v. 70, no. 4, p. 1233–1261.
- Calabro, M.D., Schmidt, D.A., and Roering, J.J., 2010, An examination of seasonal deformation at the Portuguese Bend landslide, southern California, using radar interferometry: *Journal of Geophysical Research—Earth Surface*, v. 115, F02020, doi:10.1029/2009JF001314.
- Carson, M.A., and Petley, D.J., 1970, The existence of threshold hillslopes in the denudation of the landscape: *Transactions of the Institute of British Geographers*, v. 49, p. 71–95.
- Chen, C.W., and Zebker, H.A., 2000, Network approaches to two-dimensional phase unwrapping: Intractability and two new algorithms: *Journal of the Optical Society of America, ser. A, Optics, Image Science, and Vision*, v. 17, no. 3, p. 401–414, doi:10.1364/JOSAA.17.000401.
- Chen, C.W., and Zebker, H.A., 2001, Two-dimensional phase unwrapping with use of statistical models for cost functions in nonlinear optimization: *Journal of the Optical Society of America, ser. A, Optics, Image Science, and Vision*, v. 18, no. 2, p. 338–351, doi:10.1364/JOSAA.18.000338.
- Chen, C.W., and Zebker, H.A., 2002, Phase unwrapping for large SAR interferograms: Statistical segmentation and generalized network models: *IEEE Transactions on Geoscience and Remote Sensing*, v. 40, no. 8, p. 1709–1719, doi:10.1109/TGRS.2002.802453.
- Chester, F.M., and Logan, J.M., 1986, Implications for mechanical-properties of brittle faults from observations of the Punchbowl fault zone, California: *Pure and Applied Geophysics*, v. 124, no. 1–2, p. 79–106, doi:10.1007/BF00875720.
- Clarke, B.A., and Burbank, D.W., 2010, Bedrock fracturing, threshold hillslopes, and limits to the magnitude of bedrock landslides: *Earth and Planetary Science Letters*, v. 297, no. 3–4, p. 577–586, doi:10.1016/j.epsl.2010.07.011.
- Coe, J.A., Ellis, W.L., Godt, J.W., Savage, W.Z., Savage, J.E., Michael, J.A., Kibler, J.D., Powers, P.S., Lidke, D.J., and Debray, S., 2003, Seasonal movement of the Slumgullion landslide determined from Global Positioning System surveys and field instrumentation, July 1998–March 2002: *Engineering Geology*, v. 68, no. 1–2, p. 67–101, doi:10.1016/S0013-7952(02)00199-0.
- Cruden, D.M., and Varnes, D.J., 1996, Landslide types and processes, in Turner, A.K., and Schuster, R.L., eds., *Landslides: Investigation and Mitigation*: Washington, D.C., National Academy Press, p. 36–71.
- DeLong, S.B., Prentice, C.S., Hillel, G.E., and Ebert, Y., 2012, Multitemporal ALSM change detection, sediment delivery, and process mapping at an active earthflow: *Earth Surface Processes and Landforms*, v. 37, no. 3, p. 262–272, doi:10.1002/esp.2234.
- Dibblee, T.W., 2005, Geologic Map of the Parkfield Quadrangle, Fresno and Monterey Counties: Santa Barbara, California, Santa Barbara Museum of Natural History, scale 1:24,000, 1 sheet.
- Dibblee, T.W., 2006, Geologic Map of the Smith Mountain Quadrangle, Monterey and Fresno Counties: Santa Barbara, California, Santa Barbara Museum of Natural History, scale 1:24,000, 1 sheet.
- Dibblee, T.W., 2007a, Geologic Map of the Bickmore Canyon Quadrangle, Monterey and San Benito Counties: Santa Barbara, California, Santa Barbara Museum of Natural History, scale 1:24,000, 1 sheet.
- Dibblee, T.W., 2007b, Geologic Map of the Cherry Peak Quadrangle, San Benito County: Santa Barbara, California, Santa Barbara Museum of Natural History, scale 1:24,000, 1 sheet.
- Dibblee, T.W., 2007c, Geologic Map of the Hepsedam Peak Quadrangle, Monterey and San Benito Counties: Santa Barbara, California, Santa Barbara Museum of Natural History, scale 1:24,000, 1 sheet.
- Dibblee, T.W., 2007d, Geologic Map of the Lonoak Quadrangle, Monterey and San Benito Counties: Santa Barbara, California, Santa Barbara Museum of Natural History, scale 1:24,000, 1 sheet.
- Dibblee, T.W., 2007e, Geologic Map of the Monarch Peak Quadrangle, Monterey and San Benito Counties: Santa Barbara, California, Santa Barbara Museum of Natural History, scale 1:24,000, 1 sheet.
- Dibblee, T.W., 2007f, Geologic Map of the Priest Valley Quadrangle, San Benito, Monterey and Fresno Counties: Santa Barbara, California, Santa Barbara Museum of Natural History, scale 1:24,000, 1 sheet.
- Dibblee, T.W., 2007g, Geologic Map of the Rock Spring Peak Quadrangle, San Benito County: Santa Barbara, California, Santa Barbara Museum of Natural History, scale 1:24,000, 1 sheet.

- Dibblee, T.W., 2007h, Geologic Map of the San Benito Mountain Quadrangle, Fresno, Monterey and San Benito Counties: Santa Barbara, California, Santa Barbara Museum of Natural History, scale 1:24,000, 1 sheet.
- Dibblee, T.W., 2007i, Geologic Map of the Slack Canyon Quadrangle, Monterey and Fresno Counties: Santa Barbara, California, Santa Barbara Museum of Natural History, scale 1:24,000, 1 sheet.
- Dibblee, T.W., 2007j, Geologic Map of the Stockdale Mountain Quadrangle, Monterey County: Santa Barbara, California, Santa Barbara Museum of Natural History, scale 1:24,000, 1 sheet.
- Dietrich, W.E., Reiss, R., Hsu, M.L., and Montgomery, D.R., 1995, A process-based model for colluvial soil depth and shallow landsliding using digital elevation data: *Hydrological Processes*, v. 9, no. 3–4, p. 383–400, doi:10.1002/hyp.3360090311.
- Dietrich, W.E., Bellugi, D.G., Sklar, L.S., Stock, J.D., Heimath, A.M., and Roering, J.J., 2003, Geomorphic transport laws for predicting landscape form and dynamics, in Wilcock, P.R., and Iverson, R., eds., *Prediction in Geomorphology*: Washington, D.C., American Geophysical Union.
- Dor, O., Ben-Zion, Y., Rockwell, T.K., and Brune, J., 2006, Pulverized rocks in the Mojave section of the San Andreas fault zone: *Earth and Planetary Science Letters*, v. 245, no. 3–4, p. 642–654, doi:10.1016/j.epsl.2006.03.034.
- Dor, O., Yildirim, C., Rockwell, T.K., Ben-Zion, Y., Emre, O., Sisk, M., and Duman, T.Y., 2008, Geological and geomorphologic asymmetry across the rupture zones of the 1943 and 1944 earthquakes on the North Anatolian fault: Possible signals for preferred earthquake propagation direction: *Geophysical Journal International*, v. 173, no. 2, p. 483–504, doi:10.1111/j.1365-246X.2008.03709.x.
- Fialko, Y., Sandwell, D., Agnew, D., Simons, M., Shearer, P., and Minster, B., 2002, Deformation on nearby faults induced by the 1999 Hector Mine earthquake: *Science*, v. 297, no. 5588, p. 1858–1862, doi:10.1126/science.1074671.
- Finzi, Y., Hearn, E.H., Ben-Zion, Y., and Lyakhovskiy, V., 2009, Structural properties and deformation patterns of evolving strike-slip faults: Numerical simulations incorporating damage rheology: *Pure and Applied Geophysics*, v. 166, no. 10–11, p. 1537–1573, doi:10.1007/s00024-009-0522-1.
- Gabet, E.J., Burbank, D.W., Putkonen, J.K., Pratt-Sitaula, B.A., and Ojha, T., 2004, Rainfall thresholds for landsliding in the Himalayas of Nepal: *Geomorphology*, v. 63, no. 3–4, p. 131–143, doi:10.1016/j.geomorph.2004.03.011.
- Gesch, D., 2007, The National Elevation Dataset, in Maune, D., ed., *Digital Elevation Model Technologies and Applications: The DEM User's Manual*: Bethesda, Maryland, American Society for Photogrammetry and Remote Sensing, p. 99–118.
- Gesch, D., Oimoen, M., Greenlee, S., Nelson, C., Steuck, M., and Tyler, D., 2002, The National Elevation Dataset: *Photogrammetric Engineering and Remote Sensing*, v. 68, no. 1, p. 5.
- Goldstein, R.M., and Werner, C.L., 1998, Radar interferogram filtering for geophysical applications: *Geophysical Research Letters*, v. 25, no. 21, p. 4035–4038, doi:10.1029/1998GL900033.
- Graham, R.C., Rossi, A.M., and Hubbert, K.R., 2010, Rock to regolith conversion: Producing hospitable substrates for terrestrial ecosystems: *GSA Today*, v. 20, no. 2, p. 4–9, doi:10.1130/GSAT57A.1.
- Graham, S.A., Stanley, R.G., Bent, J.V., and Carter, J.B., 1989, Oligocene and Miocene paleogeography of central California and displacement along the San Andreas fault: *Geological Society of America Bulletin*, v. 101, no. 5, p. 711–730, doi:10.1130/0016-7606(1989)101<0711:OAMPOC>2.3.CO;2.
- Hensley, S., Michel, T., Simard, M., Jones, C., Muellerschoen, R., Le, C., Zebker, H., and Chapman, B., 2009a, Residual motion estimation for UAVSAR: Implications of an electronically scanned array, in *Proceedings 2009 IEEE Radar Conference*, Pasadena, California, May 04–08, p. 450–454, doi:10.1109/RADAR.2009.4977065.
- Hensley, S., Zebker, H., Jones, C., Michel, T., Muellerschoen, R., and Chapman, B., 2009b, First deformation results using the NASA/JPL UAVSAR instrument, in *2nd Annual Asia Pacific SAR Conference*: Xian, China, doi:10.1109/APSAR.2009.5374246.
- Hilley, G.E., and Arrowsmith, J.R., 2008, Geomorphic response to uplift along the Dragon's Back pressure ridge, Carrizo Plain, California: *Geology*, v. 36, no. 5, p. 367–370, doi:10.1130/G24517A.1.
- Huffman, O.F., 1972, Lateral displacement of Upper Miocene rocks and Neogene history of offset along the San Andreas fault in central California: *Geological Society of America Bulletin*, v. 83, no. 10, p. 2913–2946, doi:10.1130/0016-7606(1972)83[2913:LDOUMR]2.0.CO;2.
- Hutchinson, J.N., and Bhandari, R.K., 1971, Undrained loading, a fundamental mechanism of mudflows and other mass movements: *Geotechnique*, v. 21, no. 4, p. 353–358, doi:10.1680/geot.1971.21.4.353.
- Iverson, R.M., 1985, A constitutive equation for mass-movement behavior: *The Journal of Geology*, v. 93, no. 2, p. 143–160, doi:10.1086/628937.
- Iverson, R.M., and Major, J.J., 1987, Rainfall, groundwater-flow, and seasonal movement at Minor Creek Landslide, northwestern California—Physical interpretation of empirical relations: *Geological Society of America Bulletin*, v. 99, no. 4, p. 579–594, doi:10.1130/0016-7606(1987)99<579:RGFASM>2.0.CO;2.
- Jennings, C.W., and Burnett, J.L., compilers, 1961, Geologic Map of California: San Francisco Sheet: State of California Department of Natural Resources, scale 1:250,000, 1 sheet.
- Keefer, D.K., 1984, Landslides caused by earthquakes: *Geological Society of America Bulletin*, v. 95, no. 4, p. 406–421, doi:10.1130/0016-7606(1984)95<406:LCBE>2.0.CO;2.
- Keefer, D.K., 2000, Statistical analysis of an earthquake-induced landslide distribution—The 1989 Loma Prieta, California, event: *Engineering Geology*, v. 58, p. 231–249, doi:10.1016/S0013-7952(00)00037-5.
- Keefer, D.K., and Johnson, A.M., 1983, Earth Flows: Morphology, Mobilization and Movement: U.S. Geological Survey Professional Paper 1264.
- Kelsey, H.M., 1978, Earthflows in Franciscan mélange, Van Duzen River basin, California: *Geology*, v. 6, no. 6, p. 361–364, doi:10.1130/0091-7613(1978)6<361:EIFMVD>2.0.CO;2.
- Korup, O., 2006, Rock-slope failure and the river long profile: *Geology*, v. 34, no. 1, p. 45–48, doi:10.1130/G21959.1.
- Larsen, I.J., and Montgomery, D.R., 2012, Landslide erosion coupled to tectonics and river incision: *Nature Geoscience*, v. 5, no. 7, p. 468–473, doi:10.1038/ngeo1479.
- Larsen, I.J., Montgomery, D.R., and Korup, O., 2010, Landslide erosion controlled by hillslope material: *Nature Geoscience*, v. 3, no. 4, p. 247–251, doi:10.1038/ngeo776.
- Lawson, A.C., compiler, 1908, The California earthquake of April 18, 1906: Report of the State Earthquake Investigation Commission, Vol. 1: Washington, D.C., Carnegie Institution of Washington Publication, 451 p.
- Leprince, S., Berthier, E., Ayoub, F., Delacourt, C., and Avouac, J.P., 2008, Monitoring Earth surface dynamics with optical imagery: Eos (Transactions, American Geophysical Union), v. 89, p. 1, doi:10.1029/2008EO10001.
- Lewis, M.A., Ben-Zion, Y., and McGuire, J.J., 2007, Imaging the deep structure of the San Andreas fault south of Hollister with joint analysis of fault zone head and direct P arrivals: *Geophysical Journal International*, v. 169, no. 3, p. 1028–1042, doi:10.1111/j.1365-246X.2006.03319.x.
- Li, Y.G., Vidale, J.E., and Cochran, E.S., 2004, Low-velocity damaged structure of the San Andreas fault at Parkfield from fault zone trapped waves: *Geophysical Research Letters*, v. 31, no. 12, L12S06, doi:10.1029/2003GL019044.
- Lienkaemper, J.J., Williams, P.L., and Guilderson, T.P., 2010, Evidence for a twelfth large earthquake on the southern Hayward fault in the past 1900 years: *Bulletin of the Seismological Society of America*, v. 100, no. 5A, p. 2024–2034, doi:10.1785/0120090129.
- Lisle, T.E., 1989, Sediment transport and resulting deposition in spawning gravels, north coastal California: *Water Resources Research*, v. 25, no. 6, p. 1303–1319, doi:10.1029/WR025i06p01303.
- Ma, S., 2008, A physical model for widespread near-surface and fault zone damage induced by earthquakes: *Geochemistry Geophysics Geosystems*, v. 9, Q11009, doi:10.1029/2008GC002231.
- Mackey, B.H., and Roering, J.J., 2011, Sediment yield, spatial characteristics, and the long-term evolution of active earthflows determined from airborne LiDAR and historical aerial photographs, Eel River, California: *Geological Society of America Bulletin*, v. 123, no. 7–8, p. 1560–1576, doi:10.1130/B30306.1.
- Mackey, B.H., Roering, J.J., and McKean, J.A., 2009, Long-term kinematics and sediment flux of an active earthflow, Eel River, California: *Geology*, v. 37, no. 9, p. 803–806, doi:10.1130/G30136A.1.
- Malamud, B.D., Turcotte, D.L., Guzzetti, F., and Reichenbach, P., 2004a, Landslide inventories and their statistical properties: *Earth Surface Processes and Landforms*, v. 29, no. 6, p. 687–711, doi:10.1002/esp.1064.
- Malamud, B.D., Turcotte, D.L., Guzzetti, F., and Reichenbach, P., 2004b, Landslides, earthquakes, and erosion: *Earth and Planetary Science Letters*, v. 229, no. 1–2, p. 45–59, doi:10.1016/j.epsl.2004.10.018.
- Manaker, D.M., Bürgmann, R., Prescott, W.H., and Langbein, J., 2003, Distribution of interseismic slip rates and the potential for significant earthquakes on the Calaveras fault, central California: *Journal of Geophysical Research—Solid Earth*, v. 108, no. B6, 20 p., doi:10.1029/2002JB001749.
- Matthews, V., 1976, Correlation of Pinnacles and Neenach Volcanic Formations and their bearing on San Andreas fault problem: *American Association of Petroleum Geologists Bulletin*, v. 60, no. 12, p. 2128–2141.
- McKean, J., and Roering, J., 2004, Objective landslide detection and surface morphology mapping using high-resolution airborne laser altimetry: *Geomorphology*, v. 57, no. 3–4, p. 331–351, doi:10.1016/S0169-555X(03)00164-8.
- McSaveney, M.J., and Griffiths, G.A., 1987, Drought, rain, and movement of a recurrent earthflow complex in New Zealand: *Geology*, v. 15, no. 7, p. 643–646, doi:10.1130/0091-7613(1987)15<643:DRAMOA>2.0.CO;2.
- Meunier, P., Hovius, N., and Haines, A.J., 2007, Regional patterns of earthquake-triggered landslides and their relation to ground motion: *Geophysical Research Letters*, v. 34, no. 20, L20408, doi:10.1029/2007GL031337.
- Meunier, P., Hovius, N., and Haines, A.J., 2008, Topographic site effects and the location of earthquake induced landslides: *Earth and Planetary Science Letters*, v. 275, no. 3–4, p. 221–232, doi:10.1016/j.epsl.2008.07.020.
- Mitchell, T.M., Ben-Zion, Y., and Shimamoto, T., 2011, Pulverized fault rocks and damage asymmetry along the Arima-Takatsuki Tectonic Line, Japan: *Earth and Planetary Science Letters*, v. 308, no. 3–4, p. 284–297, doi:10.1016/j.epsl.2011.04.023.
- Molnar, P., Anderson, R.S., and Anderson, S.P., 2007, Tectonics, fracturing of rock, and erosion: *Journal of Geophysical Research—Earth Surface*, v. 112, no. F3, 12 p., doi:10.1029/2005JF000433.
- Montgomery, D.R., 2004, Geology, geomorphology, and the restoration ecology of salmon: *GSA Today*, v. 14, no. 11, p. 4–12, doi:10.1130/1052-5173(2004)014<4:GGATRE>2.0.CO;2.
- Montgomery, D.R., and Dietrich, W.E., 1994, A physically-based model for the topographic control on shallow landsliding: *Water Resources Research*, v. 30, no. 4, p. 1153–1171, doi:10.1029/93WR02979.
- Montgomery, D.R., Schmidt, K.M., Greenberg, H.M., and Dietrich, W.E., 2000, Forest clearing and regional landsliding: *Geology*, v. 28, no. 4, p. 311–314, doi:10.1130/0091-7613(2000)28<311:FCARL>2.0.CO;2.
- Nadeau, R.M., and McEvilly, T.V., 2004, Periodic pulsing of characteristic microearthquakes on the San Andreas fault: *Science*, v. 303, no. 5655, p. 220–222, doi:10.1126/science.1090353.
- National Elevation Dataset, 2011, National Elevation Dataset, United States Geological Survey: <http://ned.usgs.gov/> (last accessed December 2011).
- Nolan, K.M., and Marron, D.C., 1985, Contrast in stream-channel response to major storms in two mountainous areas of California: *Geology*, v. 13, no. 2, p. 135–138, doi:10.1130/0091-7613(1985)13<135:CISRTM>2.0.CO;2.

- Oppenheimer, D.H., Bakun, W.H., and Lindh, A.G., 1990, Slip partitioning of the Calaveras fault, California, and prospects for future earthquakes: *Journal of Geophysical Research—Solid Earth and Planets*, v. 95, no. B6, p. 8483–8498, doi:10.1029/JB095iB06p08483.
- Ouimet, W.B., Whipple, K.X., and Granger, D.E., 2009, Beyond threshold hillslopes: Channel adjustment to base-level fall in tectonically active mountain ranges: *Geology*, v. 37, no. 7, p. 579–582, doi:10.1130/G30013A.1.
- Parker, R.N., Densmore, A.L., Rosser, N.J., de Michele, M., Li, Y., Huang, R., Whadcoat, S., and Petley, D.N., 2011, Mass wasting triggered by the 2008 Wenchuan earthquake is greater than orogenic growth: *Nature Geoscience*, v. 4, no. 7, p. 449–452, doi:10.1038/ngeo1154.
- Percia, S., and 17 others, 2011, NOAA Atlas 14: Precipitation-Frequency Atlas of the United States, California, Volume 6, Version 2.0: Silver Spring, Maryland, National Oceanic and Atmospheric Administration, National Weather Service, http://hdsc.nws.noaa.gov/hdsc/pfds/pfds_gis.html (accessed July 2012).
- PRISM Climate Group, 2011, PRISM Climate Group, Oregon State University: <http://prism.oregonstate.edu> (last accessed December 2011).
- Putnam, W.C., and Sharp, R.P., 1940, Landslides and earthflows near Ventura, Southern California: *Geographical Review*, v. 30, no. 4, p. 591–600, doi:10.2307/210535.
- Radbruch-Hall, D.H., Colton, R.B., Davies, W.E., Lucchitta, L., Skipp, B.A., and Varnes, D.J., 1982, *Landslide Overview Map of the Conterminous United States*: U.S. Geological Survey Professional Paper 1183.
- Reid, M.E., Brien, D.L., LaHusen, R.G., Roering, J.J., de la Fuente, J., and Ellen, S.D., 2003, Debris-flow initiation from large, slow-moving landslides, in Rickenmann, D., and Chen, C.-I., eds., *Debris-Flow Hazards Mitigation: Mechanics, Prediction, and Assessment*, Volumes 1 and 2, p. 155–166.
- Revenaugh, J., and Reasoner, C., 1997, Cumulative offset of the San Andreas fault in central California: A seismic approach: *Geology*, v. 25, no. 2, p. 123–126, doi:10.1130/0091-7613(1997)025<0123:COOTSA>2.3.CO;2.
- Roering, J.J., Kirchner, J.W., Sklar, L.S., and Dietrich, W.E., 2001, Hillslope evolution by nonlinear creep and landsliding: An experimental study: *Geology*, v. 29, no. 2, p. 143–146, doi:10.1130/0091-7613(2001)029<0143:HEBNCA>2.0.CO;2.
- Roering, J.J., Schmidt, K.M., Stock, J.D., Dietrich, W.E., and Montgomery, D.R., 2003, Shallow landsliding, root reinforcement, and the spatial distribution of trees in the Oregon Coast Range: *Canadian Geotechnical Journal*, v. 40, no. 2, p. 237–253, doi:10.1139/t02-113.
- Roering, J.J., Kirchner, J.W., and Dietrich, W.E., 2005, Characterizing structural and lithologic controls on deep-seated landsliding: Implications for topographic relief and landscape evolution in the Oregon Coast Range, USA: *Geological Society of America Bulletin*, v. 117, no. 5–6, p. 654–668, doi:10.1130/B25567.1.
- Roering, J.J., Stimely, L.L., Mackey, B.H., and Schmidt, D.A., 2009, Using DInSAR, airborne LiDAR, and archival air photos to quantify landsliding and sediment transport: *Geophysical Research Letters*, v. 36, L19402, doi:10.1029/2009GL040374.
- Rogers, T.H., compiler, 1966, *Geologic Map of California: San Jose Sheet*: State of California Department of Natural Resources, scale 1:250,000, 1 sheet.
- Rolandone, F., Bürgmann, R., Agnew, D.C., Johanson, I.A., Templeton, D.C., d'Alessio, M.A., Titus, S.J., DeMets, C., and Tikoff, B., 2008, Aseismic slip and fault-normal strain along the central creeping section of the San Andreas fault: *Geophysical Research Letters*, v. 35, no. 14, p. L14305, doi:10.1029/2008GL034437.
- Rosen, P.A., Hensley, S., Joughin, I.R., Li, F.K., Madsen, S.N., Rodriguez, E., and Goldstein, R.M., 2000, Synthetic aperture radar interferometry—Invited paper: *Proceedings of the IEEE*, v. 88, no. 3, p. 333–382, doi:10.1109/5.838084.
- Ryder, I., and Bürgmann, R., 2008, Spatial variations in slip deficit on the central San Andreas fault from InSAR: *Geophysical Journal International*, v. 175, no. 3, p. 837–852, doi:10.1111/j.1365-246X.2008.03938.x.
- Rymer, M.J., Tinsley, J.C., III, Treiman, J.A., Arrowsmith, J.R., Clahan, K.B., Rosinski, A.M., Bryant, W.A., Snyder, H.A., Fuis, G.S., Toke, N.A., and Bawden, G.W., 2006, Surface fault slip associated with the 2004 Parkfield, California, earthquake: *Bulletin of the Seismological Society of America*, v. 96, no. 4B, p. S11–S27, doi:10.1785/0120050830.
- Savage, H.M., and Brodsky, E.E., 2011, Collateral damage: Evolution with displacement of fracture distribution and secondary fault strands in fault damage zones: *Journal of Geophysical Research—Solid Earth*, v. 116, 14 p, doi:10.1029/2010JB007665.
- Savage, J.C., and Burford, R.O., 1973, Geodetic determination of relative plate motion in central California: *Journal of Geophysical Research*, v. 78, no. 5, p. 832–845, doi:10.1029/JB078i005p0832.
- Schmidt, K.M., Roering, J.J., Stock, J.D., Dietrich, W.E., Montgomery, D.R., and Schaub, T., 2001, The variability of root cohesion as an influence on shallow landslide susceptibility in the Oregon Coast Range: *Canadian Geotechnical Journal*, v. 38, no. 5, p. 995–1024, doi:10.1139/t01-031.
- Schulz, W.H., McKenna, J.P., Kibler, J.D., and Biavati, G., 2009, Relations between hydrology and velocity of a continuously moving landslide—Evidence of pore-pressure feedback regulating landslide motion?: *Landslides*, v. 6, no. 3, p. 181–190, doi:10.1007/s10346-009-0157-4.
- Schwab, M., Rieke-Zapp, D., Schneider, H., Liniger, M., and Schlunegger, F., 2008, Landsliding and sediment flux in the central Swiss Alps: A photogrammetric study of the Schimbrig landslide, Entlebuch: *Geomorphology*, v. 97, no. 3–4, p. 392–406, doi:10.1016/j.geomorph.2007.08.019.
- Simons, M., and Rosen, P.A., 2007, Interferometric synthetic aperture radar geodesy, in Schubert, G., ed., *Treatise on Geophysics*, Volume 3: Elsevier, p. 391–446.
- Swanson, F.J., and Swanson, D.N., 1977, Complex mass-movement terrains in the western Cascade Range, Oregon: *Geological Society of America Reviews in Engineering Geology*, v. 3, p. 113–124.
- Thurber, C., Roecker, S., Ellsworth, W., Chen, Y., Lutter, W., and Sessions, R., 1997, Two-dimensional seismic image of the San Andreas fault in the northern Gabilan range, central California: Evidence for fluids in the fault zone: *Geophysical Research Letters*, v. 24, no. 13, p. 1591–1594, doi:10.1029/97GL01435.
- Titus, S.J., DeMets, C., and Tikoff, B., 2005, New slip rate estimates for the creeping segment of the San Andreas fault, California: *Geology*, v. 33, no. 3, p. 205–208, doi:10.1130/G21107.1.
- Trotter, C.M., 1993, Weathering and regolith properties at an earthflow site: *Quarterly Journal of Engineering Geology*, v. 26, no. 3, p. 163–178, doi:10.1144/GSL.QJEGH.1993.026.003.02.
- Tucker, G.E., and Hancock, G.R., 2010, Modelling landscape evolution: *Earth Surface Processes and Landforms*, v. 35, no. 1, p. 28–50, doi:10.1002/esp.1952.
- Unsworth, M., Egbert, G., and Booker, J., 1999, High-resolution electromagnetic imaging of the San Andreas fault in central California: *Journal of Geophysical Research—Solid Earth*, v. 104, no. B1, p. 1131–1150, doi:10.1029/98JB01755.
- van Asch, T.W.J., 2005, Modelling the hysteresis in the velocity pattern of slow-moving earth flows: The role of excess pore pressure: *Earth Surface Processes and Landforms*, v. 30, no. 4, p. 403–411, doi:10.1002/esp.1147.
- Wechsler, N., Rockwell, T.K., and Ben-Zion, Y., 2009, Application of high resolution DEM data to detect rock damage from geomorphic signals along the central San Jacinto fault: *Geomorphology*, v. 113, no. 1–2, p. 82–96, doi:10.1016/j.geomorph.2009.06.007.
- Western Regional Climate Center, 1986, NOAA Cooperative Stations: <http://www.wrcc.dri.edu/climatedata/climsum/> (last accessed December 2011).
- Western Regional Climate Center, 2011, Cooperative Climatological Data Summaries: <http://www.wrcc.dri.edu/climatedata/climsum/> (accessed February 2011).
- Wieczorek, G.F., Reid, M.E., Jodicke, W., Pearson, C., and Wilcox, G., 2007, Rainfall and Seasonal Movement of the Weeks Creek Landslide, San Mateo County, California: U.S. Geological Survey Data Series 278.
- Zhang, X.B., Phillips, C., and Marden, M., 1993, A comparison of earthflow movement mechanisms on forested and grassed slopes, Raukumara Peninsula, North Island, New Zealand: *Geomorphology*, v. 6, no. 2, p. 175–187, doi:10.1016/0169-555X(93)90045-4.

SCIENCE EDITOR: A. HOPE JAHREN
ASSOCIATE EDITOR: SHANAKA DE SILVA

MANUSCRIPT RECEIVED 1 MAY 2012
REVISED MANUSCRIPT RECEIVED 1 OCTOBER 2012
MANUSCRIPT ACCEPTED 2 OCTOBER 2012

Printed in the USA